INFRARED IMAGING OF HIGH-REDSHIFT GALAXIES

by

Brian Andrew McLeod

A Dissertation Submitted to the Faculty of the

DEPARTMENT OF ASTRONOMY

In Partial Fulfillment of the Requirements
For the Degree of

DOCTOR OF PHILOSOPHY

In the Graduate College

THE UNIVERSITY OF ARIZONA

1 9 9 4

Order Number 9517595

Infrared imaging of high-redshift galaxies

McLeod, Brian Andrew, Ph.D.

The University of Arizona, 1994

U·M·I

300 N. Zeeb Rd.
Ann Arbor, MI 48106

INFRARED IMAGING OF HIGH-REDSHIFT GALAXIES

by

Brian Andrew McLeod

A Dissertation Submitted to the Faculty of the

DEPARTMENT OF ASTRONOMY

In Partial Fulfillment of the Requirements
For the Degree of

DOCTOR OF PHILOSOPHY

In the Graduate College

THE UNIVERSITY OF ARIZONA

1 9 9 4

THE UNIVERSITY OF ARIZONA
GRADUATE COLLEGE

As members of the Final Examination Committee, we certify that we have read the dissertation prepared by Brian Andrew McLeod entitled Infrared Imaging of High-Redshift Galaxies

and recommend that it be accepted as fulfilling the dissertation requirement for the Degree of Doctor of Philosophy

Dr. Marcia J. Rieke	Date 9/2/94
Dr. Christopher D. Impey	Date 9/2/94
Dr. Robert C. Kennicutt, Jr.	Date 9-2-94
Dr. Donald W. McCarthy, Jr.	Date 9/2/94
	Date

Final approval and acceptance of this dissertation is contingent upon the candidate's submission of the final copy of the dissertation to the Graduate College.

I hereby certify that I have read this dissertation prepared under my direction and recommend that it be accepted as fulfilling the dissertation requirement.

Marcia J. Rieke — 9/2/94

Dissertation Director
Dr. Marcia J. Rieke

Date

STATEMENT BY AUTHOR

This dissertation has been submitted in partial fulfillment of requirements for an advanced degree at The University of Arizona and is deposited in the University Library to be made available to borrowers under rules of the Library.

Brief quotations from this dissertation are allowable without special permission, provided that accurate acknowledgment of source is made. Requests for permission for extended quotation from or reproduction of this manuscript in whole or in part may be granted by the head of the major department or the Dean of the Graduate College when in his or her judgment the proposed use of the material is in the interests of scholarship. In all other instances, however, permission must be obtained from the author.

SIGNED: Brian A. McLeod

ACKNOWLEDGMENTS

I would like to thank Eric Tollestrup and Giovanni Fazio for obtaining the MMT time and assisting with those observations in Chapter 2. Gary Bernstein assisted with the observations and with making the initial catalogs for the bright-end data. He also served as my chief FOCAS consultant. David Koo and Caryl Gronwall provided their redshift and color data to me for the modeling chapter. Gustavo Bruzual supplied the galaxy evolution code that is central to the models. Hy Spinrad and Mark Dickinson were the source of the list of radio galaxies studied in Chapter 4. They were always quick to answer my various email questions.

Kim McLeod assisted with the figures and tables in Chapter 4. Thanks also go to her, along with the AAS, for providing the LaTeX macros that formatted this document. Because of her, this document required no hand modifications, appearing exactly as it came out of the laser printer.

A number of people provided distractions from this work. Though they may have slowed me down somewhat, at least I enjoyed graduate school more as a result. The ACME adaptive optics group, particularly Peter Wizinowich, David Wittman, Mike Lloyd-Hart, and D'nardo Colucci, provided lots of fun times in the lab and at the telescope. I would like to thank string quartet players Ned Bloomfield, Anne Denny & Marilyn Pierce for welcoming me into their group. Evenings with them and the Southern Arizona Symphony were welcome breaks from the daily astronomy routine.

Several faculty members were especially important. Roger Angel is always an inspiration with his endless fountain of ideas. Don McCarthy has been my mentor almost since I got here, always willing to take the time to give good advice or just chat. Marcia Rieke, my advisor, jumped in with these projects when it became clear that the time was not quite ripe to do extragalactic astronomy with adaptive optics. She also generously allowed me to use her office and computer for the past several months as I finished up this work. And despite how it may have looked, I was *not* actually shackled to the chair in her office.

Gary Bernstein served as a sounding board numerous times during our time at Steward. Thanks, Gary, for cheerfully listening to all my latest modeling trials and tribulations and for being a good friend.

And finally thanks to my family: to my parents, Bob & Margot, for encouraging curiousity from day one; to my cats, Hobie & Angus, for being furry; and especially to my wife, Kim, for being my friend and love.

Contents

List of Figures

List of Tables

ABSTRACT

First we present new infrared counts of field galaxies from more than 20 square arcminutes to a limiting magnitude of K=20 and from 2 square arcminutes to K=21.5. At the faintest magnitudes the counts are slightly higher than those reported previously, though still consistent given the small numbers of galaxies in the two samples.

Next we present models predicting the magnitude, redshift and color distributions of field galaxies. We explore whether a fading starburst scenario can account for the observations of faint blue galaxies. We marginally rule out a starburst scenario with a local IMF because the models predict too many nearby faint galaxies that are not observed. A burst model with a truncated IMF reproduces the counts and redshift distributions well but produces too blue a population. We show that surface brightness selection has a significant effect on the distributions. In particular, adding a population of low-surface brightness galaxies, known to exist locally, can explain the counts for $B_J < 23$. Finally we show that the colors of galaxies in a K-band selected sample are not consistent with a passive evolution model.

In the final section we consider the effects of radio power on a sample of galaxies around $z = 1$. We have obtained $BRJHK$ images of 25 galaxies from the MIT-Green Bank (MG) radio survey. Compared with a sample of more powerful 3CR radio galaxies, these galaxies are 0.5 mag fainter when measured in 8″ apertures but not noticeably fainter in 4″ apertures. This implies that the near environments of galaxies are correlated with radio power. The MG sample contains galaxies that are just as blue as the bluest 3CR galaxies, but the median MG galaxy is slightly redder than the median 3CR galaxy at the same redshift.

Chapter 1

INTRODUCTION

1.1 Field Galaxies

A powerful test of our understanding of galaxy evolution and cosmology lies in understanding the observed properties of galaxies over as large a range of wavelengths and magnitudes as possible. We wish to create a model which specifies the basic cosmological parameters (q_0 and H_0) and a description of the distribution of the physical properties of galaxies, i.e., their spectra, luminosities, and sizes. A complete description must also include the time-dependence of these properties. From this description we can then predict observable properties: the distribution of apparent magnitudes, colors, and redshifts. Since we cannot directly observe the evolution of individual galaxies, our understanding of evolution can be tested only through changes in the populations of galaxies.

Hubble (1936) showed that the number of galaxies per magnitude interval, $n(m)$, followed the relation $d\log n/dm = 0.6$ for bright galaxies, as predicted by simple theory. A detailed derivation of $n(m)$ as a function of q_0 was done by

Sandage (1961;1988), who showed that, to first order, $n(m)$ is independent of q_0. The importance of galaxy evolution was shown by Brown & Tinsley (1974) who pointed out that "a meaningful interpretation of the $N(m)$ relation will require good estimates of the luminosity functions, spectral energy distributions and evolution of a wide range of types of galaxies." However, the sophistication of the models to explain the observed distributions remained relatively simple until recently, partly due to a lack of observational constraints.

Early determinations (e.g. Peterson et al. 1979) showed that $n(m)$ in the blue had a slope consistent with moderate amounts of luminosity evolution. The interpretation that steep slope implies luminosity evolution was made in the absence of redshift distributions, $n(z)$, and it came as a surprise to many when the excess galaxies turned out to be at fairly low redshifts (Broadhurst et al. 1988). An additional puzzle came with deep K-band field counts (Cowie 1991; Gardner et al. 1993), which showed no excess of galaxies over that predicted by a simple no-evolution model.

There have been several approaches to explaining the apparent discrepancy between the simple models and the observations. One possibility is the addition of a population of starbursting galaxies (Lilly et al. 1991) with the number of bursting galaxies increasing with redshift. These galaxies have since faded, been disrupted or merged. Broadhurst et al. (1991) addressed the merging scenario with a model that combined merging with substantial luminosity evolution to match the K and B_J counts and B_J redshift distributions. However, it is not clear that the present population of galaxies can account for the required merger products (Dalcanton 1994). Yoshii (1993) has recently argued that introducing a non-zero cosmological constant is sufficient to bring the models into agreement. On the other hand, gravitational lensing statistics severely constrain the cosmological constant

(Maoz & Rix 1993). Koo & Kron (1992) and Koo, Gronwall, & Bruzual (1993) have argued that the local luminosity function is not sufficiently well known to rule out models with no merging and no new populations. They present a no-evolution model that fits a large range of observables, but at the expense of removing nearly all the luminous red galaxies from the local luminosity function.

1.2 Radio Galaxies

Because most faint galaxies are moderate luminosity galaxies at moderate redshifts, finding high-redshift galaxies based on optical and IR properties is very difficult. Most known high-redshift galaxies were found because they contain powerful radio sources. As such, radio-selected galaxies provide one of the only sources of stellar populations for study at high redshift. A serious concern is whether these radio galaxies are representative of the class of high-redshift galaxies, or whether the radio sources have a profound effects on the galaxies they inhabit. Most earlier work on high redshift galaxies has concentrated on the now well-studied 3CR sample (Bennet 1962). Infrared aperture photometry (e.g. Lilly & Longair, 1984; Eisenhardt & Lebofsky 1987; Lebofsky & Eisenhardt 1986) showed that the Hubble diagram (redshift vs. apparent magnitude) exhibits a very tight correlation in the IR. As one goes to higher redshift the correlation remains tight but deviates slightly to brighter apparent magnitudes, as would be expected with passive stellar evolution.

The tightness of the K-Hubble diagram led some to advocate that radio-selected galaxies have well determined properties and would be good tools for studying galaxy evolution and cosmology at high redshift (e.g., Lilly 1989). The discovery of the "alignment effect" (McCarthy et al. 1987; Chambers et al.

1987) put somewhat of a damper on this optimism. They noticed that in some high-redshift objects the visible wavelength emission was aligned with the radio axis. This meant that radio source at the center had a serious impact on the galaxy as a whole. Perhaps radio galaxies were not representative of galaxies generally after all.

Early infrared imaging of high redshift 3CR galaxies (Eisenhardt & Chokshi 1990) suggested that the alignment effect extended into the infrared, though the galaxies studied were biased towards more active ones. Rigler et al. (1992) greatly expanded the number of IR images of 3CR galaxies with a multiwavelength imaging study of 13 galaxies with $0.8 < z < 1.3$. They concluded that the alignment effect was much weaker in the IR, and fit a 2-component model to their galaxies: a round component plus a linear component. This analysis showed that the linear component contributed less than 10% to the IR flux of the galaxy.

A more recent study (Dunlop & Peacock 1993) has expanded the IR sample yet again. Their study consists of 19 3CR galaxies and additional sample of 14 galaxies from the Parkes Selected Regions (PSR) survey. This second sample has galaxies with lower radio fluxes ($S_{2.7\,\mathrm{GHz}} > 100\,\mathrm{mJy}$). They concluded that the galaxies in the low-luminosity sample are redder and rounder than the high-luminosity galaxies. A shortcoming of this sample is the lack of spectroscopic redshifts so they can provide no information on the absolute K magnitudes of their galaxies. For a list of other surveys underway, see the review by McCarthy (1993).

1.3 Objectives

The goal of the first section of this dissertation is to make an independent observational determination of the field galaxy counts for $16 < K < 21.5$. Since the

faint infrared counts provide an important constraint to models, it is important to have an independent confirmation of the University of Hawaii results (Gardner et al. 1993). A description of the observations, reductions, and results is given in Chapter 2.

In Chapter 3 we consider the implications of the observed galaxy magnitude, color, and redshift distributions. In beginning this project we set out to evaluate the various types of models without preconceived biases. With such a complex problem, only a limited set of scenarios can be considered. Here we restrict ourselves to zero cosmological constant and we do not consider galaxy merging. We concentrate on evaluating the effects of adding a fading starburst population and considering surface-brightness selection effects. The evolution properties of the galaxies are constrained by stellar-evolution models, i.e. no arbitrary luminosity evolution of galaxies will be allowed (e.g. Lilly 1993). We also try to evaluate each model with a large number of observational constraints.

Finally we explore the effects of radio power on galaxies at high redshift. The sample under study here is similar to the PSR sample in its radio properties, with the important difference that our sample has redshifts. We selected galaxies with redshifts between 0.8 and 2.0. We mainly concentrate here on those galaxies with redshifts around 1.0. These galaxies match in redshift with the Rigler et al. (1992) sample, but have significantly lower radio powers. We will investigate the optical and IR properties of radio galaxies as a function of radio power. In particular we consider the absolute K luminosities of these galaxies and their optical-IR colors.

Chapter 2

K-BAND GALAXY COUNTS

We present new counts of field galaxies from two surveys. The first covers more than 20 square arcminutes and has a limiting magnitude of K=20. The second covers 2 square arcminutes to K=21.5. At the faintest magnitudes the counts are slightly higher than those reported previously, though still consistent given the small numbers of galaxies in the two samples.

2.1 Introduction

Attempts to learn about galaxy evolution and cosmology by studying the numbers of galaxies as a function of apparent magnitude have been underway now for several decades. Substantial progress has been made in the past few years as electronic detectors have become rapidly larger and more sensitive (see review by Koo & Kron 1992). Until recently, studies of faint field galaxies had been limited to optical wavelengths. These studies showed a larger and larger excess of galaxies compared with simple models as one looked at fainter magnitudes. This led to some

speculation that a large amount of luminosity evolution had occurred in the past, causing us to see large numbers of high-redshift galaxies. Recent redshift surveys of blue–selected galaxies have since shown that the excess galaxies are not at high redshift (Colless et al. 1993). Furthermore, studies of K-band counts with IR arrays have shown that the excess of galaxies is not present at longer wavelengths.

Most of the deep IR imaging surveys of faint galaxies to date have been carried out at the University of Hawaii. Their observational results are summarized by Gardner et al. (1993). More recently, Soifer et al. (1994) presented results obtained with the Keck telescope showing somewhat higher counts though these are of fields surrounding high-redshift objects and may contain unknown numbers of associated galaxies. Because the faint K-band counts provide an important constraint to models, we set out to provide independent confirmation of the earlier results. In this chapter we present new observations made of four different fields: two small but deep fields and two wider but shallower fields. The wider fields are also serving as the starting point for a redshift survey selected to K=19.

2.2 Observations

2.2.1 Faint end

Counts for K>20 were determined from two fields taken at the Multiple Mirror Telescope (MMT) using a 128 × 128 NICMOS2 array camera with 0.″44 pixels. The two fields, which we call SA57MMT and LynxMMT, are subsets of fields previously observed by Elston et al. (1990) to K = 18. Individual exposures were 60 s long. Each exposure was shifted in position randomly from the previous one to fill a 20″ × 20″ box subject to the constraint that adjacent exposures were

not closer than 10″ to each other. The images were taken through the 2MASS K_s 2.00–2.35μm filter (see Table 2.1). Details of the observations are listed in Table 2.2.

Due the unique geometry of the telescope, IR imaging at the MMT has two added complications not found at conventional telescopes. First, the camera has a cold pupil stop with six holes to match the entrance pupil of the telescope. Because the instrument must be rotated below the telescope to compensate for field rotation, the stop inside the dewar must be counter-rotated. This is accomplished using a simple stepper motor on the outside of the dewar encoded with a potentiometer. The position of the stop is updated at the beginning of each exposure. This maintains adequate alignment except when observing near the zenith, where the parallactic angle changes rapidly.

The second complication is the need to keep the images from the six mirrors aligned. This stacking process is done directly with the IR array controlling the telescope's secondary mirrors, using the same general procedure as the MMT's Telescope Coalignment System (Montgomery & Janes 1986). The images are restacked every third exposure. This conservative procedure guaranteed that the image quality did not degrade more than 0.″1 between image stackings.

Table 2.1. K_s Filter

Microns	Transmission	Microns	Transmission
1.90.....	0.000	2.20.....	0.900
1.95.....	0.005	2.25.....	0.910
2.00.....	0.700	2.30.....	0.860
2.05.....	0.860	2.35.....	0.070
2.10.....	0.890	2.40.....	0.000
2.15.....	0.885		

2.2.2 Bright end

The data used to determine galaxy counts from K_s=17–20 were obtained at the Steward Observatory 1.55m Catalina telescope using the Steward NICMOS3 256 × 256 camera with 0.″914 pixels. One field, SA57SO, was selected from a Kitt Peak 4m photographic field of the north galactic pole. The particular area we chose was based solely on the criterion that it have a few stars sufficiently bright to be used for registering the individual short exposures. The second field, Her-1, had been previously imaged at optical wavelengths (Bernstein et al., in preparation). Again the details are summarized in Table 2.2. A total of 6 hours integration was obtained for each of the two fields. Additionally, we have 3 hours at J band on the SA57SO field. Complementary CCD images of the SA57SO field were obtained at B_J at the Steward Observatory Kitt Peak 2.3m telescope on UT 1993 Apr 17. CCD images of the Her-1 field at B_J, R and I were obtained previously by G. Bernstein at the Kitt Peak 4m telescope.

Table 2.2. Summary of Observations

Field Name	α(1950)	δ(1950)	Filter	Time	Image Size	Telescope	Detector	UT Dates
LynxMMT	08:45:12.6	+44:55:33	K_s	44160s	0.44"×128	MMT	NICMOS2	1992 Dec 6-7
								1993 Mar 6-9
SA57MMT	13:06:57.0	+29:34:54	K_s	41880s	0.44"×128	MMT	NICMOS2	1993 Mar 5-10
SA57SO ..	13:07:17.6	+29:25:01	K_s	19080s	0.9"×256	SO1.55m	NICMOS3	1993 Mar 30-31
								1993 Apr 2
			J	10800s	0.9"×256	SO1.55m	NICMOS3	1993 Apr 1
			B_J	21600s	0.3"×1024	SO2.3m	Loral2k	1993 Apr 17
Her-1	17:20:39.4	+50:04:48	K_s	13500s	0.9"×256	SO1.55m	NICMOS3	1993 Mar 30-31
								1993 Apr 1-2
			I	6600s	0.47"×1024	KP4m	TEK1	1991 Jun 18
			R	8700s	0.47"×1024	KP4m	TEK1	1991 Jun 15
			B_J	8100s	0.47"×1024	KP4m	TEK1	1991 Jun16

2.3 Data Reduction

The images were reduced in a conventional manner. For each infrared image, a local sky image constructed from the median of the six temporally nearest images was subtracted. The images were flat fielded using the median of all the images taken of that field on a given night. A further illumination correction was determined by measuring the brightness of a single star on an 11×11 grid of positions on the array. This correction is necessary because not all background photons reaching the detector (e.g. telescope thermal emission) necessarily traveled through the same path as the photons from the star. Thus the flat-field image does not represent the true response of the system to focused starlight. The correction is of order 10% at the Catalina telescope and up to 30% at the MMT due to vignetting in the beam-combining optics.

The MMT images were then shifted by integer pixel amounts determined solely from the offsets sent to the telescope mount. The Catalina images were shifted with linear interpolation with the shifts determined from bright stars in each frame. The images were averaged using a sigma-clipping algorithm to reject bad pixels and cosmic rays. The combined MMT images have a FWHM of $1\farcs2$; the Catalina images, $2\farcs1$.

2.4 Image Analysis

2.4.1 Detection and photometry

The combined images were then processed with FOCASv3.3 (Valdes 1982; Jarvis & Tyson 1981) to detect the galaxies. We used the default 5×5 pixel

triangular smoothing filter {(0,1,2,1,0),(1,2,3,2,1),(2,3,4,3,2),(1,2,3,2,1),(0,1,2,1,0)} with a detection threshold of 3 sigma per pixel and a minimum detection area of 6 pixels. The corresponding surface brightness thresholds are K=22.9 magnitudes per square arcsecond for the SA57MMT image and K=23.1 for LynxMMT, SA57SO, and Her-1. Despite similar limiting isophotes, fainter galaxies are detected on the MMT images because the minimum area is 1.2 arcsec^2 versus 5.0 arcsec^2 on the Catalina images. The magnitudes derived are the FOCAS "total" magnitudes: the detected isophotal area is doubled before the flux is summed. To determine the completeness of the detection process we generated 1000 $\times$ 1000 pixel simulated images with the same noise properties as the original images. The images were filled with objects with the same PSF as the true image and having the same magnitude distribution but extended to the faint end. A completeness correction, presented below, was determined by taking the ratio of the input to the derived distributions. Because the completeness correction was determined using simulated point sources, this provides a lower limit to the true count of finite-sized galaxies.

The photometry was referenced to the standards of Elias et al. (1982). We detect no color term for the K_s filter compared with the Elias stars. For the MMT data the frames were referenced to the nearby stars used for stacking the images and calibration of these stars was done at the Catalina telescope. This eliminated the need to spend time on standards at the MMT and skirted the problem that the Elias standards are too bright for easy use on a large telescope.

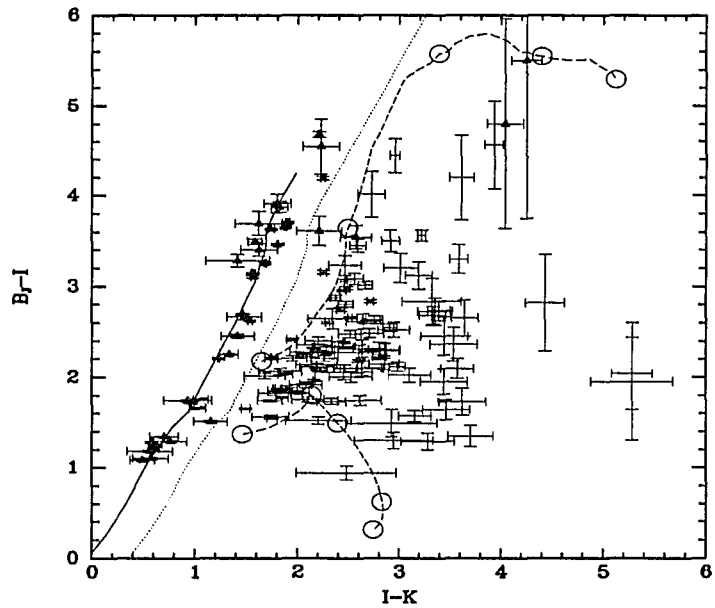

Fig. 2.1.—
Color-color diagram of the Her-1 field. The triangles denote unresolved objects. The solid line shows the main sequence and we classify as stars everything to the left of the dotted line. The upper dashed line shows the location of an old population galaxy from z=0 to z=2. Intervals of 0.5 in z are indicated by open circles. The lower dashed line is for a constant star-formation model.

2.4.2 Star-galaxy separation

Star-galaxy discrimination was done on the Catalina images based on color. Colors of the objects were measured by transforming all the images to the same scale and smoothing to the same resolution. Isophotes determined from the K image were then overlayed on the other images and fluxes were measured. Figure 2.1 shows a color-color diagram for the Her-1 field. The solid line indicates the locus of the main sequence using colors from Johnson (1966) and the transformation $B_J - R = 1.2(B - V) + 0.04$ (Gullixson et al. 1995). We also consider the sizes of

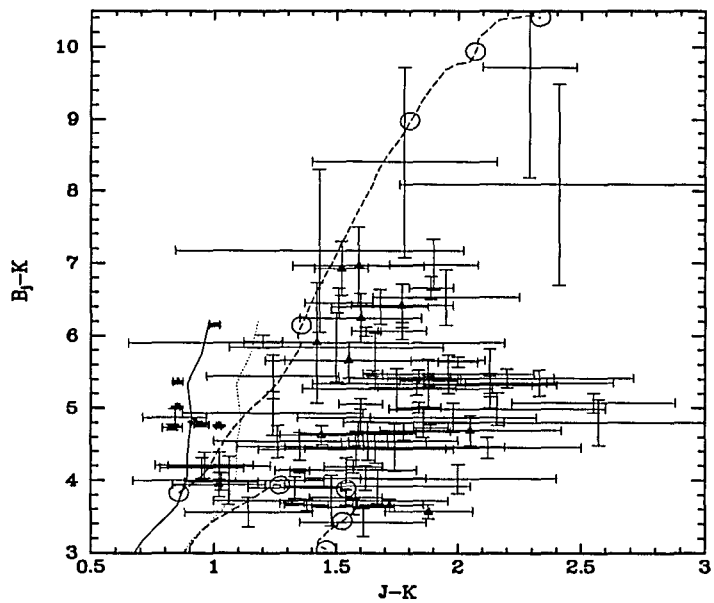

Fig. 2.2.—

Color-color diagram of the SA57SO field. The notation is the same as in Figure 2.1.

the objects measured on the R image, which had the best seeing (1.″2 FWHM). The triangles indicate unresolved objects (FOCAS scale parameter < 1.1). With just a few exceptions, the unresolved objects are well separated in color-color space. We classify as stars all the objects to the left of the dashed line, which is the $I - K$ color of the main sequence plus 0.4. Figure 2.2 shows the corresponding diagram for the SA57SO field with resolution information from the 1.″3 FWHM B_J image. Because the J image is not as deep as the Her-1 I image, the separation is not as clean. There is a clear locus of unresolved objects at the left side however. Because the J data were taken under conditions that were not quite photometric, we have also adjusted the zero-point of the $J - K$ data so that the unresolved objects lie

on top of the main-sequence curve. We adopt as stellar all the objects blueward of $J - K$ of the main sequence plus 0.2.

At fainter magnitudes contamination by stars is less of a problem. The number of stars at the galactic pole can be estimated from the models of Bahcall & Soniera (1981). Assuming a mean $I - K$ color of 2.0, their model predicts at the galactic pole a contamination level of roughly 10% at K=19.5 falling to 2% by K=21.5. This result is confirmed by extrapolating the K-band model of Wainscoat et al. (1992). Because the contamination level is small we have performed no star-galaxy separation on the MMT data.

2.5 Results and Discussion

Tables 2.3–2.5 list sample entries from the MMT, Her-1, and SA57SO catalogs respectively. The complete catalogs, to $K = 20$ (Catalina) and $K = 21.5$ (MMT), will be published on the AAS CDROM Volume 4. The astrometry for the Her-1 and MMT fields was referenced to the Hubble Space Telescope Guide Star Catalog. The SA57SO field astrometry was determined using the Minnesota Automated Plate Scan (Pennington et al. 1993) accessed via ADS [1]. The errors on the magnitudes and colors were determined by measuring the variance of the sky pixels around each object and scaling to the size of the aperture used. Errors on the $X - K$ colors are often smaller than the K errors because the colors were measured in smaller apertures than the K magnitudes. Systematic errors in the zero-points may contribute an additional few hundredths of a magnitude.

The resulting raw and corrected counts are listed in Table 2.6. Figure 2.3

[1]NASA's Astrophysical Data System v4.0

Table 2.3. Sample of MMT Catalog

ID	$\alpha(2000)$	$\delta(2000)$	K	σ_K
MMTL-8	8:48:38.12	44:44:36.6	19.35	0.11
MMTS-1	13:09:21.65	29:19:21.2	18.23	0.06
MMTS-6	13:09:19.90	29:19:12.6	21.18	0.24

Table 2.4. Sample of Her-1 Catalog

ID	Class	$\alpha(2000)$	$\delta(2000)$	K	σ_K	$I-K$	σ_{I-K}	$R-I$	σ_{R-I}	B_J-I	σ_{Bj-I}
1	t	17:21:48.29	50:00:46.7	13.66	0.01	1.31	0.00	0.74	0.00	1.13	0.00
79	g	17:22:03.41	50:02:37.8	18.36	0.16	2.10	0.16	0.59	0.02	1.75	0.03
87	s	17:21:51.85	50:02:15.9	18.71	0.23	1.80	0.13	1.63	0.02	3.91	0.10
127	g	17:21:48.02	50:01:28.7	19.29	0.24	2.16	0.17	0.94	0.02	2.35	0.04

Note. — Class codes (based on colors) are: g = Galaxy; s = Star; t = Star saturated on CCD frames, colors are incorrect.

Table 2.5. Sample of SA57SO Catalog

ID	Class	$\alpha(2000)$	$\delta(2000)$	K	σ_K	$J-K$	σ_{J-K}	B_J-K	σ_{Bj-K}
17	s	13:09:42.72	29:09:17.1	17.52	0.08	0.83	0.04	4.73	0.04
44	g	13:09:35.93	29:10:29.2	18.71	0.19	1.68	0.20	6.40	0.24
88	g	13:09:33.82	29:10:18.5	19.32	0.25	1.50	0.44	5.84	0.48

Note. — Class codes (based on colors) are: g = Galaxy; s = Star.

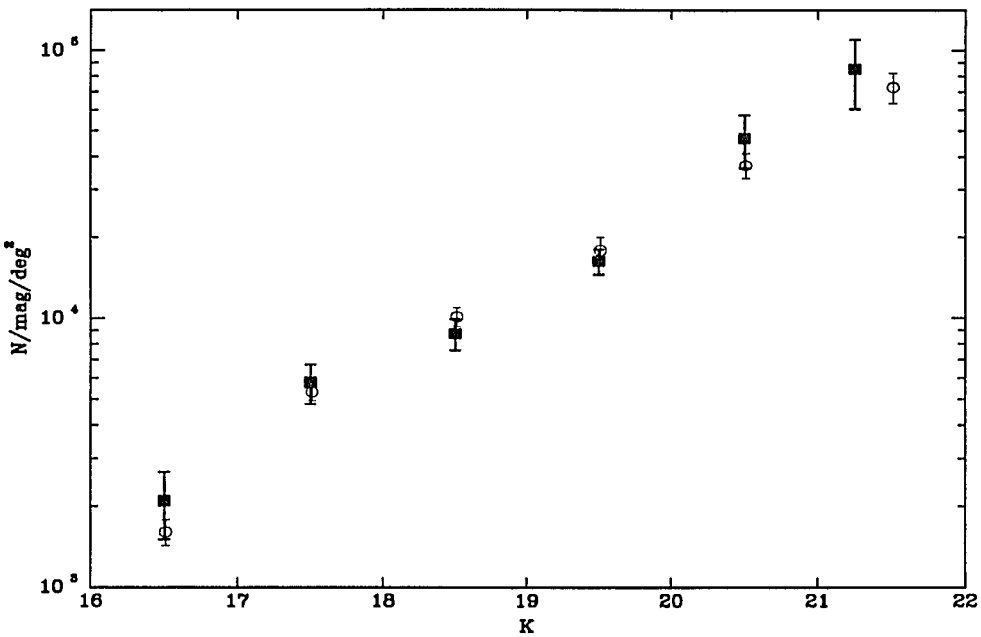

Fig. 2.3.—
K-band corrected galaxy counts. Squares are data presented here; circles are from Gardner et al. (1993). The error bars represent root-N statistics.

shows our corrected counts as well as previously derived counts (Gardner et al. 1993). The agreement is quite good with the possible exception of the faintest bin where our results are slightly higher. Given the size of the error bars, though, it is not clear that this deviation is significant. We measure a slope of 0.32 in the counts from K=18–22, compared with 0.26 derived by Gardner. Our results are consistent with their conclusion of a turnover in the slope around K=17. Recent results from the Keck telescope (Soifer et al. 1994) also give counts that are slightly higher than those presented by Gardner. However, the Keck counts come from fields that are very close to known high-redshift objects and the amount of contamination from associated galaxies is not clear. Further observations, particularly at the faint end,

are clearly warranted, as that is where the total number of galaxies detected is smallest, but where one gets the greatest leverage for constraining models.

In Figures 2.1 and 2.2 we have also plotted the expected colors of two types of galaxies as a function of redshift. The upper of these two evolving models (Bruzual & Charlot 1993) is for a galaxy that formed all of its stars in a 1 Gyr burst starting 13.5 Gyr ago (q_0=0.05; H_0=60 km s^{-1} Mpc^{-1}). The other is for constant star formation beginning 13.5 Gyr ago. The tracks span z=0–2 from left to right. The colors of most of the galaxies in Figure 2.1 are easily explained by their being normal galaxies with redshifts less than 1. However there are a few objects with $I-K>4$ or $B_J-I>4$ that are interesting. The objects red in both $I-K$ and B_J-I could be high redshift galaxies, but those red only in $I-K$ are not easily explained by tracks of normal galaxy evolution. Unfortunately, these objects all have $B_J>25$ so further investigation with optical spectroscopy will be quite difficult. Further discussion of the color distributions is presented in the next chapter.

Table 2.6. K Counts

	Bright[a]		Faint[b]		
K_s	N[c]	Completeness	N[c]	Completeness	log n[d]
16–17.....	13	1.0	...	...	3.32
17–18.....	36	1.0	...	...	3.76
18–19.....	54	1.0	4	1.0	3.94
19–20.....	78	0.77	9	1.0	4.21
20–21.....	...	...	20	0.77	4.67
21–21.5....	...	...	12	0.5	4.93

[a]Area = 22.5 sq. min.
[b]Area = 2.0 sq. min.
[c]Number of galaxies detected in the specified magnitude range
[d]Number of galaxies per square degree per magnitude

Chapter 3

MODELING OF MAGNITUDE, COLOR AND REDSHIFT DISTRIBUTIONS

3.1 Introduction

We begin with a brief description of the distributions to be computed. In § 3.3 we present a compilation of previous observational results. Section 3.4 considers a simple model with a quiescently evolving population. The next section introduces starburst populations to examine their effects on the excess blue counts. This is followed by a discussion of surface brightness effects in § 3.6 including the effects of known low surface brightness galaxies. We conclude with the implications that the $I-K$ colors of a K-selected sample have on evolution around z=1.

3.2 Theory

We consider three basic types of distributions: 1) number of galaxies as a function of apparent magnitude for a given filter; 2) number of galaxies as a function of redshift in a particular apparent magnitude range; and 3) number of galaxies as a function of color in a particular apparent magnitude range. The first quantity, the number-magnitude relation, is given by

$$n(m) = \sum_i \int_0^{z_{form}} \phi_i(M(m,z)) \frac{dV}{dz} dz. \tag{3.1}$$

The sum is over galaxies of different spectral types, ϕ_i is the luminosity function for galaxy type i, and the volume element, dV/dz, is determined by the cosmology. The relation between apparent and absolute magnitude is given by

$$M = m - 5\log\frac{d_L(z)}{10\,\mathrm{pc}} - 2.5\log\frac{(1+z)\int_0^\infty S_i(\lambda, t(z=0))F(\lambda)d\lambda}{\int_0^\infty S_i(\frac{\lambda}{1+z}, t(z))F(\lambda)d\lambda} - \Delta_i(M,z), \tag{3.2}$$

where d_L is the luminosity distance, S is the spectrum of the galaxy as a function of time, F is the filter transmission, and Δ is the aperture correction. The third term, the KE correction, is due to two effects: the redshift of the galaxy shifts the observed bandpass to a bluer and narrower range of emitted wavelengths (k-correction), and the spectrum of the galaxy changes with time (evolution). For now we will assume that $\Delta = 0$, i.e., the observed magnitude measures the total flux from the galaxy. This will be discussed further below.

The number of galaxies in a given redshift and magnitude bin is

$$n(z_l, z_u) = \sum_i \int_{z_l}^{z_u} \int_{m_l}^{m_u} \phi_i(M(m,z)) dm \frac{dV}{dz} dz. \tag{3.3}$$

The color distributions are determined by performing the integrals over magnitude and redshift, but at each step of the integration the color of the galaxy is determined and the luminosity function value is added to the appropriate color bin.

3.3 Data

Numerous observations of galaxy count vs. magnitude have been made. To obtain the best estimate of the number of galaxies at each apparent magnitude, we have combined the observations of several authors. Each data point is an average of the available data, weighted by the area surveyed. We present data only where the total number of galaxies observed is greater than 20. Data for U, B_J ($B_J = B - 0.3(B-V)$), Gunn-r, I, and K are presented in Tables 1–5, respectively. The sources are drawn from the lists in the recent review by Koo & Kron (1992) and the K-band summary by Gardner et al. (1993). Additional K data are from Chapter 2. In some cases the data to be combined were made through somewhat different filters so we have applied the color transformations given by the authors. Note that the zero point for r is based on an F-star spectrum (Thuan & Gunn 1976) and so differs from the normal A0-star normalization in that r is 0.43 mag larger than expected. The counts are from photographic surveys for $U < 22$, $B_J < 23.5$, $r < 22.0$, and $I < 21.0$; fainter counts are from CCD surveys.

3.4 Quiescent Population

We use the evolution models of Bruzual & Charlot (1993) to produce galaxy spectral energy distributions (SEDs). In all cases we have assumed a Salpeter (1955) initial mass function (IMF), i.e, $dn(m)/dm \propto m^{-2.35}$. Each of the models consists of two components: an instantaneous burst at t=0 plus a constant star formation rate (SFR) thereafter. By adjusting the ratio of the strength of the burst to the constant component we can affect the shape of the SED. The ratios were chosen so the models at an age of 13.5 Gyr would match the optical SEDs in

Table 3.1. U-band counts

U	$\log n\,[\mathrm{deg}^{-2}]$	N	Ref
18.25	1.46	31	1,2
18.75	1.67	44	1,2
19.25	1.90	70	1,2
19.75	2.23	150	1,2
20.25	2.47	260	1,2
20.75	2.66	540	1,2
21.25	2.92	420	1
21.75	3.27	920	1
22.25	3.68	170	3,4
22.75	4.04	140	3,4
23.25	4.33	280	3,4
23.75	4.54	450	3,4
24.25	4.74	720	3,4
24.75	4.85	530	4

References. — (1) Koo (1986); (2) Jones et al. (1991); (3) Majewski (1989); (4) Guhathakurta et al. (1990).

Table 3.2. B_J-band counts

B_J	$\log n\,[\mathrm{deg}^{-2}]$	N	Ref
14.25	−0.24	55	1,2
14.75	−0.21	60	1,2
15.29	−0.03	800	3
15.77	0.21	1400	3
16.25	0.48	2600	3
16.71	0.76	4900	3
17.29	1.08	10000	3
17.74	1.37	20000	3
18.29	1.69	42000	3
18.72	1.92	71000	3
19.25	2.21	140000	3
19.77	2.44	240000	3
20.27	2.66	400000	3
20.77	2.91	690000	3
21.25	3.14	2200	4
21.75	3.37	3800	4
22.25	3.60	6400	4
22.75	3.82	11000	4
23.25	4.04	17500	4
23.5	4.15	2000	5,6,7
24.0	4.42	3800	5,6,7
24.5	4.58	5100	5,6,7
25.0	4.76	2600	5
25.5	4.96	3600	5,8
26.0	5.12	4100	5,8
26.5	5.30	120	8

References. — (1) Ciardullo (1987); (2) Heydon-Dumbleton et al. (1989); (3) Maddox et al. (1990); (4) Jones et al. (1991); (5) Tyson (1988); (6) Metcalfe et al. (1991); (7) Neuschaefer et al. (1991); (8) Lilly et al. (1991).

Table 3.3. r-band counts

r	$\log n\,[\mathrm{deg}^{-2}]$	N	Ref
15.25	0.97	1800	2,3
15.75	1.17	3000	1,2,3
16.25	1.40	5200	1,2,3
16.75	1.63	8800	1,2,3
17.25	1.87	15000	1,2,3
17.75	2.12	27000	1,2,3
18.25	2.33	42000	2,3
18.75	2.55	69000	2,3
19.25	2.83	1400	1,8
19.75	3.05	2400	1,8
20.25	3.24	3700	1,8
20.75	3.42	5600	1,8
21.25	3.59	8300	1,8
21.75	3.75	12000	1,8
22.25	3.94	660	4,5,6,7
22.75	4.13	930	4,6,7
23.25	4.30	450	4,6
23.75	4.56	830	4,6
24.25	4.73	1200	4,6
24.75	4.95	1500	6
25.25	5.17	1900	6

References. — (1) Stevenson et al. (1986); (2) Sebok (1986); (3) Picard (1991); (4) Hall & Mackay (1984); (5) Yee et al. (1986); (6) Tyson (1988); (7) Metcalfe et al. (1991); (8) Jones et al. (1991).

Table 3.4. I-band counts

I	$\log n\,[\mathrm{deg}^{-2}]$	N	Ref
17.55	1.99	21	1
18.05	2.39	52	1
18.55	2.65	220	1
19.05	2.90	400	1
19.55	3.17	700	1
20.05	3.39	1200	1
20.55	3.56	1800	1
21.25	3.93	320	2,3
21.75	4.13	500	2,3
22.25	4.29	440	4,2
22.75	4.43	610	4,2
23.25	4.59	850	4,2
23.75	4.81	1200	2,5
24.25	4.98	1700	2,5
24.75	5.04	31	5

References. — (1) Koo (1986); (2) Tyson (1988); (3) Hintzen et al (1991); (4) Hall & Mackay (1984); (5) Lilly et al. (1991).

Table 3.5. K-band counts

K	$\log n\,[\mathrm{deg}^{-2}]$	N	Ref
11.5	−0.04	32	1
12.25	0.45	49	1
13.5	1.16	23	2
14.5	1.90	146	2,3
15.5	2.62	155	2,3
16.5	3.10	491	2,3
17.5	3.71	232	2,4
18.5	3.99	207	2,4
19.5	4.23	158	2,4
20.5	4.59	104	2,4
21.5	4.88	74	2,4

References. — (1) Mobasher et al. (1986); (2) Gardner et al (1993); (3) Glazebrook et al (1993); (4) McLeod et al (1994).

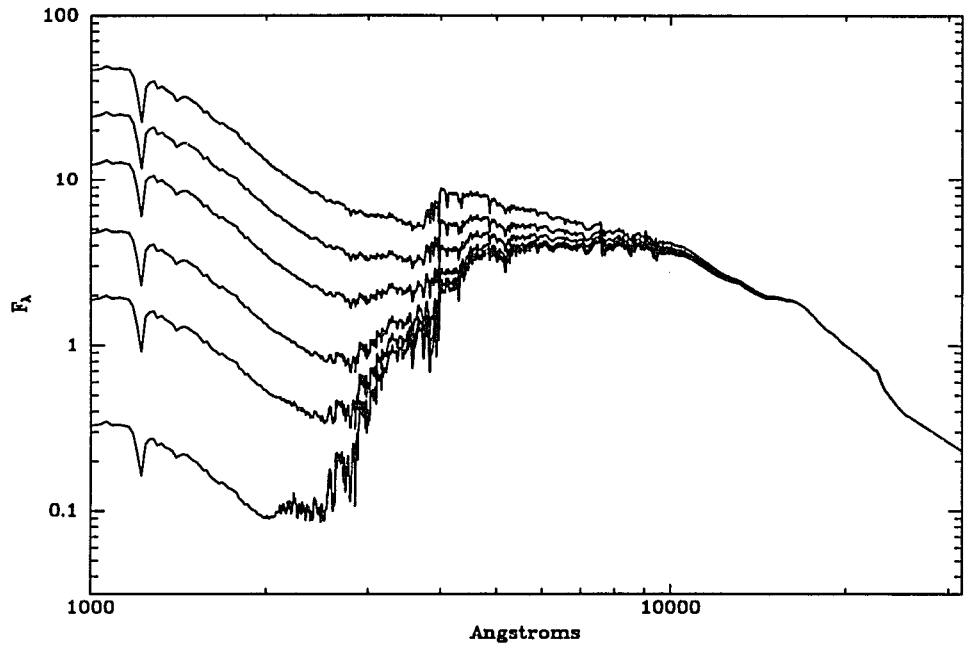

Fig. 3.1.—
Galaxy spectral energy distributions at an age of 13.5 Gyr generated by Bruzual & Charlot (1993) galaxy evolution models. From top to bottom, the star-formation rate per Gyr relative to the initial burst is 1.0, 0.03, 0.01, 0.003, 0.001, 0.00001.

Coleman, Wu, and Weedman (1980) with a near-infrared extension (Rieke & Rieke, in preparation) appended. Table 3.6 lists the amount of star formation per Gyr relative to the initial burst. Figure 3.1 shows these SEDs. The early-type galaxies are completely dominated by the initial burst; the late-type galaxies are dominated by the constant component. Figure 3.2 shows a comparison of the expected counts using the Bruzual SEDs vs. the Coleman et al. SEDs. This Bruzual model assumes that there is no evolution of the SEDs with time, an unphysical assumption, but necessary for this purpose because the Coleman et al. SEDs contain no evolutionary information. The purpose of this figure is to illustrate the order of magnitude of the errors in the counts due to uncertainties in the SEDs. Most of the divergence

Table 3.6. Quiescent population luminosity functions

Type	SFR[a]	$B-V$	Schechter parameters [b]		
			$\phi^*[\mathrm{Mpc}^{-3}\,\mathrm{mag}^{-1}]$	$M^*_{B_J}$	α
E	0.00001	0.94	1.92×10^{-4}	−21.1	−0.7
S0	0.001	0.90	1.92×10^{-4}	−21.1	−0.7
Sab	0.003	0.83	1.92×10^{-4}	−21.1	−0.7
Sc	0.01	0.7	2.60×10^{-4}	−21.4	−1.1
Sdm	0.03	0.57	0.85×10^{-4}	−21.5	−1.5
Im	1.0	0.42	0.85×10^{-4}	−21.5	−1.5

[a]Constant SFR Gyr^{-1} relative to initial burst
[b]Shanks (1990); $H_0 = 50\,\mathrm{km\,s^{-1}\,Mpc^{-1}}$

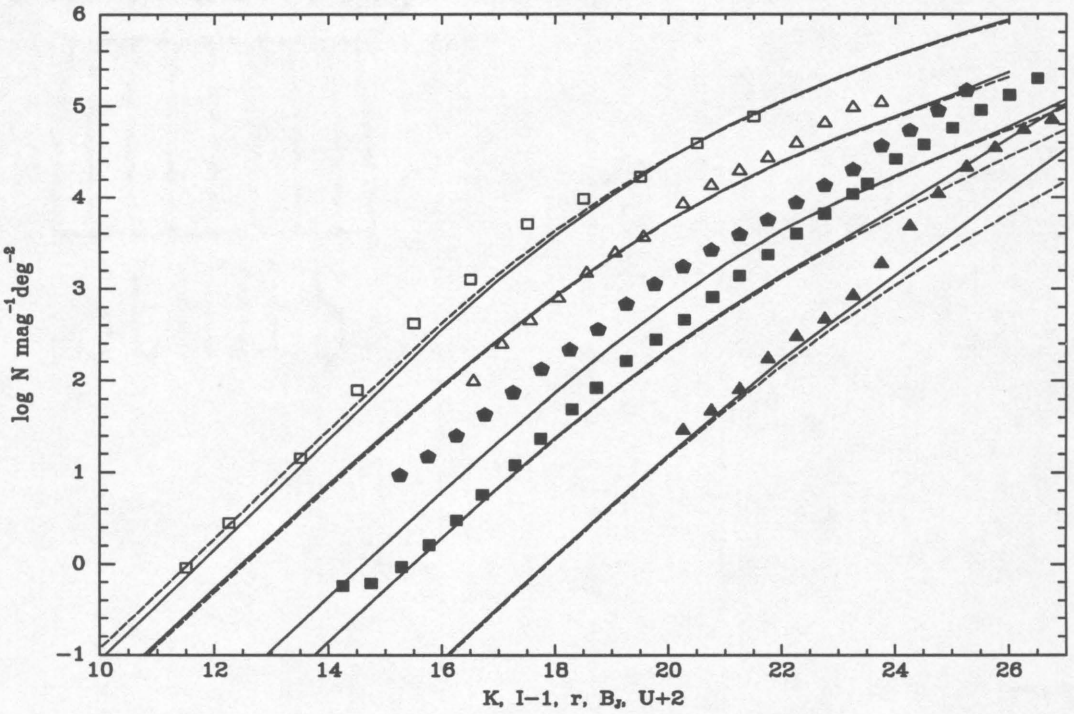

Fig. 3.2.—
Comparison of expected counts using non-evolving Bruzual SEDs (solid) vs Coleman et al. SEDs (dashed). The biggest differences occur in the faint B_J and U counts where redshifted UV flux is detected. Data plotted is listed in Tables 3.1–3.5.

occurs in the faint blue counts where the lack of understanding of the ultraviolet spectra of galaxies becomes important.

We initially consider two different local luminosity functions (LFs). The first set, used by Lilly (1993), are the type-dependent LFs presented by Bingelli, Sandage, and Tammann (1988), slightly adjusted to sum to a Schechter function with parameters $\phi^* = 0.00175\,\mathrm{Mpc}^{-3}\,\mathrm{mag}^{-1}$, $M^*_{B_J} = -21.0$, and $\alpha = -1.15$. The Schechter function (Schechter 1976) is defined by $\phi(M) = 0.92\phi^* \exp\{-0.92(M - M^*)(\alpha + 1) - \exp[-0.92(M - M^*)]\}$. This total LF is the one derived by Loveday et al. (1992), but with a slightly steeper faint end slope. All LF specifications in this paper are scaled to $H_0 = 50\,\mathrm{km\,s^{-1}\,Mpc^{-1}}$ for easy comparison with other authors. We pair each morphological type LF with the corresponding Bruzual SED. The second luminosity function we consider is the color-dependent derivation by Shanks (1990). This LF is divided into three classes, $B - V < 0.65$, $0.65 < B - V < 0.85$, and $B - V > 0.85$. Each class is further arbitrarily divided equally among different SEDs which fall within that class as shown in Table 3.6. The overall normalization of the LFs is chosen so as to match the observed counts at B_J=17. Figure 3.3 shows a comparison of the resulting color distributions of bright ($15 < B_J < 17$) galaxies from the two LFs along with the observed distribution presented in Koo & Kron (1992). The Lilly LF produces too few blue galaxies relative to red ones, while the Shanks LF has a more correct distribution. Ideally we would like a LF with more than three divisions according to color, but for now we will adopt the Shanks local LF.

In Figure 3.4 we show the resulting counts through the U, B_J, r, I and K filters. From above, we assume that the present day age of the quiescent population is 13.5 Gyr. The value of H_0 was chosen so that the galaxies are not formed at too low a redshift. For example, $H_0 = 50\,\mathrm{km\,s^{-1}\,Mpc^{-1}}$ puts the redshift of formation

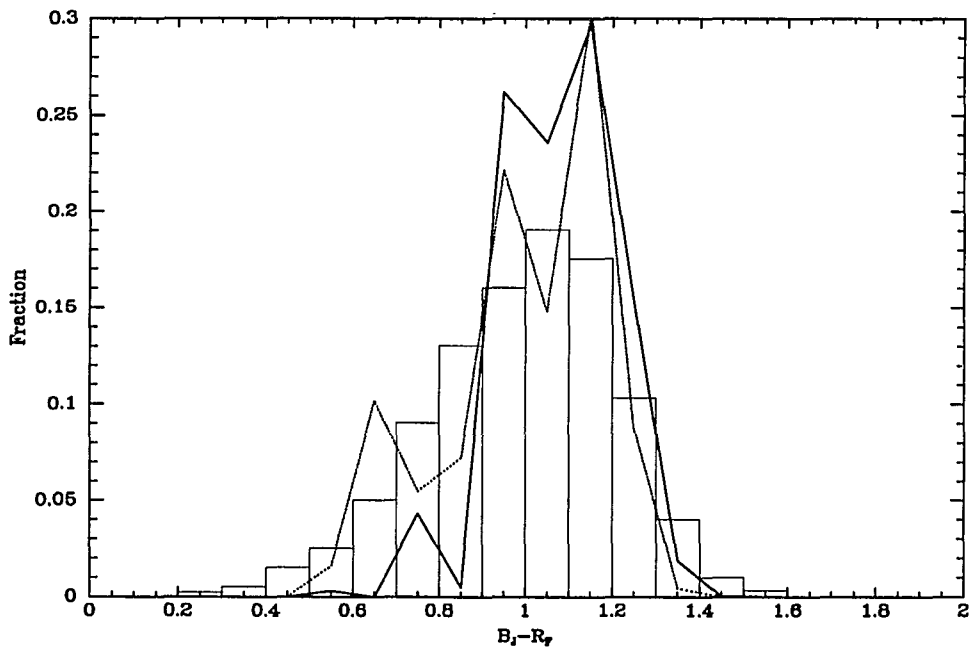

Fig. 3.3.—
Comparison of predicted color distributions ($B_J - R_F$) for bright galaxies ($15 < B_J < 17$) with observations. Transformations are $B_J = B - 0.3(B - V)$ and $R_F = R - 0.06(B - R)$. The histogram is observations from Koo & Kron (1992). The solid line shows the Lilly (1993) type-dependent LF. The dashed line shows the Shanks color-dependent LF. We prefer the Shanks LF because the colors match the observations better.

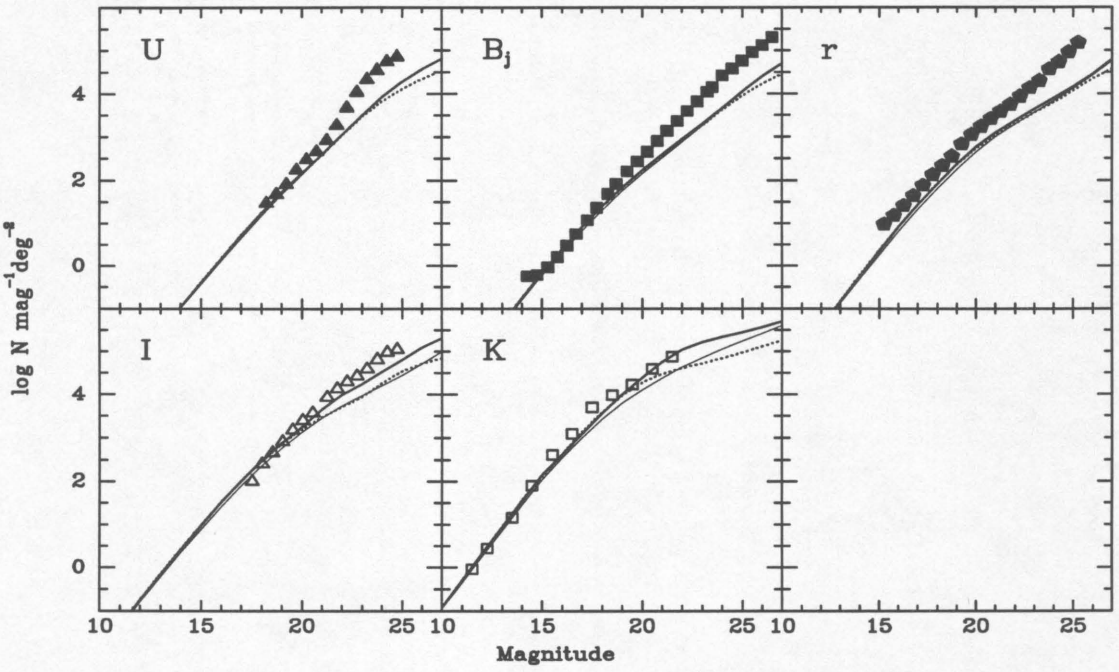

Fig. 3.4.—
Galaxy numbers vs. magnitude for simple models. The thin line shows the unphysical non-evolving model. The solid line is the passively evolving population with q_0=0.05 and $H_0 = 60\,\mathrm{km\,s^{-1}\,Mpc^{-1}}$. The dashed line is the same with q_0=0.5 and $H_0 = 47\,\mathrm{km\,s^{-1}\,Mpc^{-1}}$. The redshift of galaxy formation is z=7.3 in both cases.

at $z = 2.5$, which would be excluded by the redshift distributions (galaxies in their initial burst would be seen at relatively bright magnitudes). We have adopted z=7.3 and assume q_0=0.05, which leads to a choice of $H_0 = 60\,\mathrm{km\,s^{-1}\,Mpc^{-1}}$.

This baseline model (solid lines) shows the same basic feature of galaxy count models made by various previous authors: the simple model matches the K-band counts reasonably well, but drastically underestimates the faint blue counts. All the models show a significant discrepancy with the bright-end r observations. The reason for this is not clear. One possibility is that our SEDs are somehow drastically wrong in the r band. This seems unlikely since the Coleman et al. SEDs in Figure 3.2 produce the same effect. Secondly, the observations could have a zero-point error; or it could be a true large scale structure effect. Picard (1991) sees 30% differences between his northern and southern fields which he attributes to structure. His observations are a factor of two higher than those of Sebok (1986). These discrepancies will require independent confirmation.

The dashed line of Figure 3.4 shows the same evolutionary model for $q_0 = 0.5$. To preserve the present day SED ages of 13.5 Gyr with $z_{form} = 7.3$ we have changed H_0 to 47. The only effect of changing H_0 in these models is to change the relation of age to redshift. Figure 3.5 shows B_J-selected redshift distributions from Koo, Gronwall, & Bruzual (1993) with the predictions of the q_0=0.05 model superimposed. As in Koo et al. (1993), the histograms are shown in seven logarithmic bins per decade. Unlike other authors, we have normalized the observed redshift distributions to match the observed total number of galaxies in each magnitude interval rather than the predicted number. The ratio of the area under the histogram to that under the model curve in each panel should correspond to the prediction in the $n(m)$ plot. Thus it is easy to see from the redshift distributions that the model underpredicts the number of galaxies present for faint B_J.

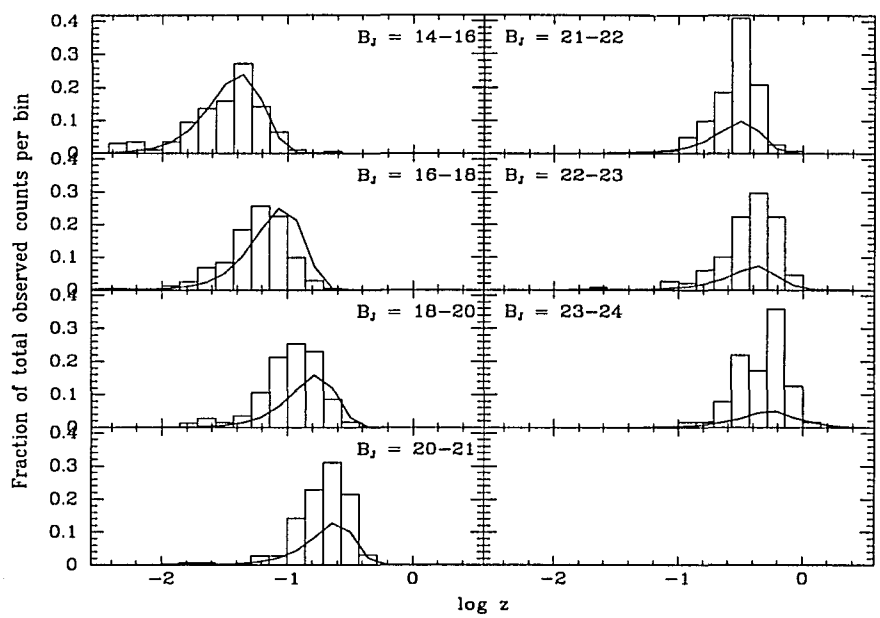

Fig. 3.5.—
Redshift distributions for the baseline passively evolving model ($q_0 = 0.05$, $H_0 = 60\,\mathrm{km\,s^{-1}\,Mpc^{-1}}$, $t = 13.5\,\mathrm{Gyr}$). The solid line is the model prediction. The histograms are the observations presented in Koo et al. 1993. The models are not normalized so that the ratio of the number of predicted galaxies at each magnitude relative to the number observed (Figure 3.4) is preserved.

3.5 Starburst Populations

In this section we consider the effects of making up for the deficiency of faint blue galaxies by adding a population of starburst galaxies. We assume that each new galaxy has a single burst of star formation lasting 0.1 Gyr and thereafter fades quiescently. This type of population should provide the largest amount of fading possible and test whether such galaxies can account for an excess of blue galaxies. For computational reasons we add the bursts at discrete points in time, one burst population for each of the observed redshift distribution bins.

The luminosity functions of the burst galaxies are determined empirically. By subtracting the baseline-model redshift distributions from the observed distributions we get the number of excess galaxies in each bin. A further division by the comoving volume of the redshift bin converts to a spatial density and one more normalization corrects for the fact that the burst galaxies are in their bright phase for only a portion of the time represented by the redshift bin they are in. We assume an effective lifetime of the burst phase of 0.2 Gyr, i.e the time for the stars to form and fade by a factor of e. The KE-correction and distance modulus determine the peak absolute magnitudes required to produce the observed apparent magnitudes. The characteristics of the burst population are tabulated in Table 3.7 and the derived burst rate LFs are shown in Figure 3.6. There are no obvious trends of the derived LFs as a function of redshift. A fit done by eye shows that Schechter parameters of $B_J^* = -19.0$, $\phi^* = 0.02\,\mathrm{Mpc}^{-3}\,\mathrm{mag}^{-1}\,\mathrm{Gyr}^{-1}$, and $\alpha = -1$ are a reasonable fit to the ensemble of LFs. Here we have normalized the amplitide ϕ^* in terms of the rate of burst formation per Gyr. Note that since the absolute magnitudes are measured at the brightest phase, a galaxy with $M_{B_J} = -19.0$ has a mass of $2 \times 10^8\,M_\odot$, a factor of 100 less massive than an old galaxy of the same

Table 3.7: Burst characteristics for 0.1–125$M_\odot$ IMF

z	Present Age (Gyr)	ΔM^a	μ^b
0.10-0.14	2.0	4.3	26.1
0.14-0.19	2.6	4.7	26.4
0.19-0.27	3.4	5.0	26.7
0.27-0.37	4.3	5.2	26.9
0.37-0.51	5.5	5.5	27.2
0.51-0.72	6.7	5.6	27.3
0.72-1.00	8.0	5.7	27.4

[a]Amount of fading between peak brightness and present.

[b]Present day central surface brightness so that $10^8 M_\odot$ burst has r_e = 3kpc.

luminosity would have.

Figures 3.7–3.9 (solid lines) show the magnitude, redshift, and color distributions for a burst model where the bursts have an IMF identical to the baseline population (Salpeter, $0.1 - 125\ M_\odot$). Now the blue counts fit reasonably well up to B_J=24. They turn over at fainter magnitudes because we have no redshift distributions at fainter levels and have made no attempt to extrapolate the burst population. The $B_J - R_F$ color distributions now show an excess at the blue end but still a deficit at the red end. The most serious concern is the redshift distributions. Although the high-z end of each distribution fits well, this model predicts a low-z tail in the $B_J > 20$ distributions that is not seen in the observations. This effect is due to the fact that the low-mass stars are long-lived

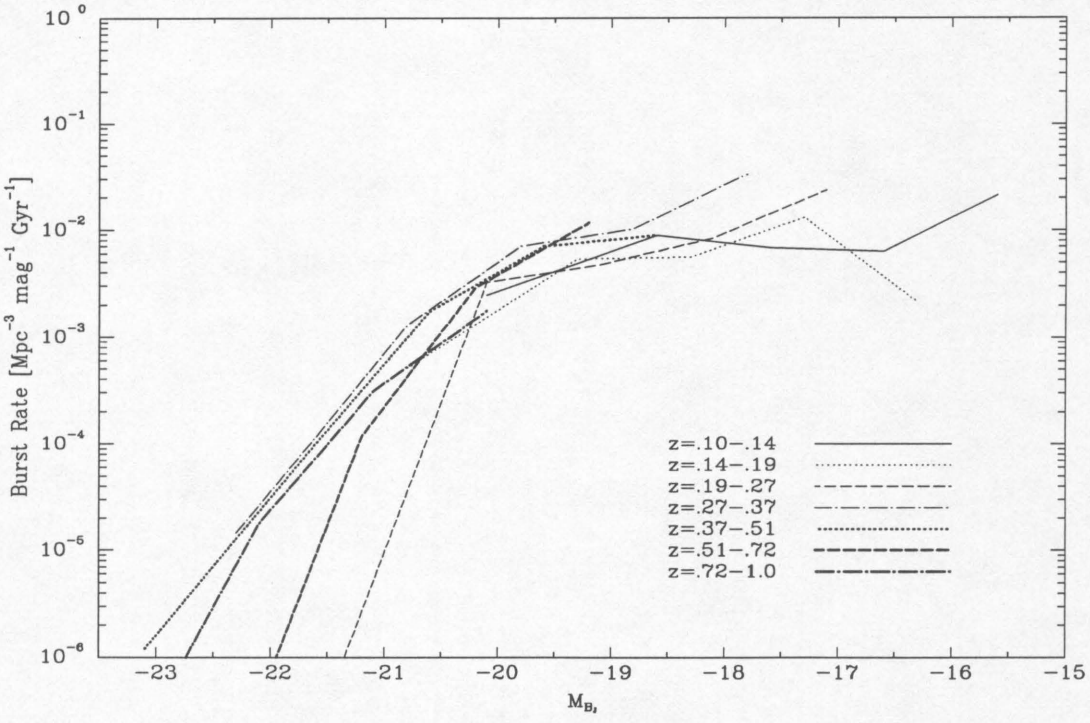

Fig. 3.6.—
Derived burst rate luminosity functions for 0.1 Gyr burst populations. The IMF is Salpeter for 0.1-125$M_{\odot}$; $H_0 = 50\,\mathrm{km\,s^{-1}\,Mpc^{-1}}$. The horizontal axis is the peak B_J absolute magnitude. The vertical axis is scaled in terms of the number of galaxies that reach the specified peak magnitude per unit comoving volume per Gyr.

and so the galaxy never fades completely. This effect is under-represented in this model since we have not added $z > 1$ bursts. In § 3.6 we will consider whether surface brightness selection effects can reduce the low redshift tail.

Modeling of the stellar populations of the nearby starburst galaxy M82 (Rieke et al. 1992) suggests that while the slope of the IMF in M82 may be equal to that of the local IMF, very few low-mass stars are produced. We now consider a starburst model using a Salpeter IMF but truncated so that no stars with $M < 2.5M_{\odot}$ are produced. An application of the Bruzual & Charlot (1993) models to this type of IMF is presented by Charlot et al. (1993). The LFs derived are identical to the

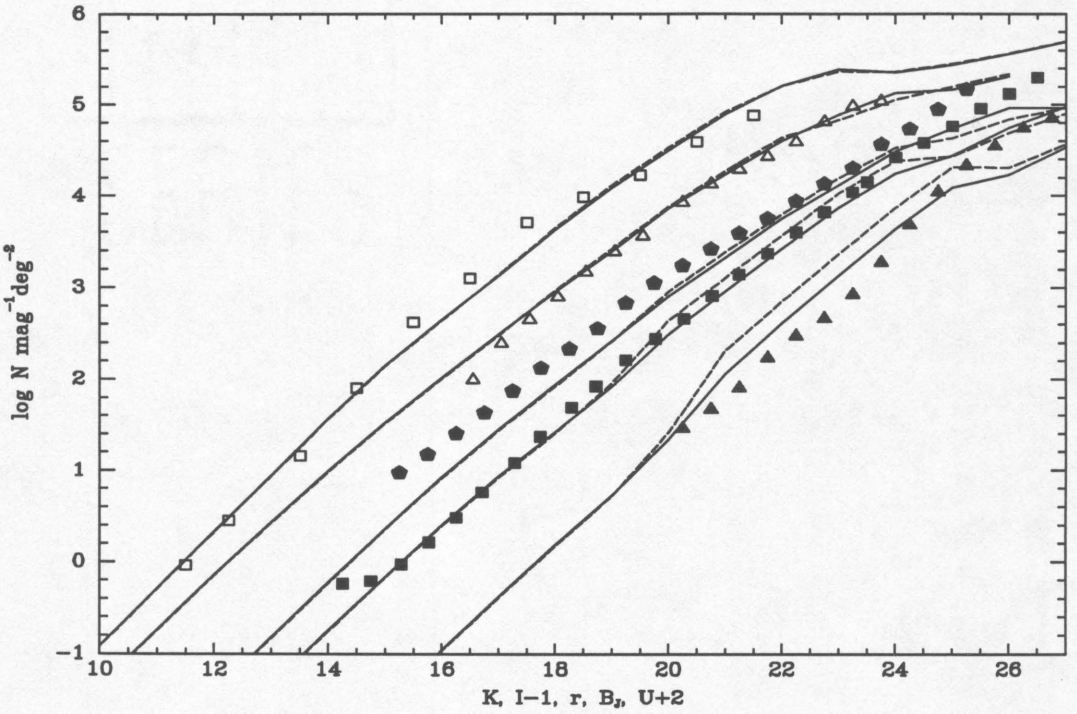

Fig. 3.7.—
Number vs. mag for burst populations. Solid line is for $0.1 - 125\ M_\odot$ IMF. Dashed line is for $2.5 - 125\ M_\odot$ IMF.

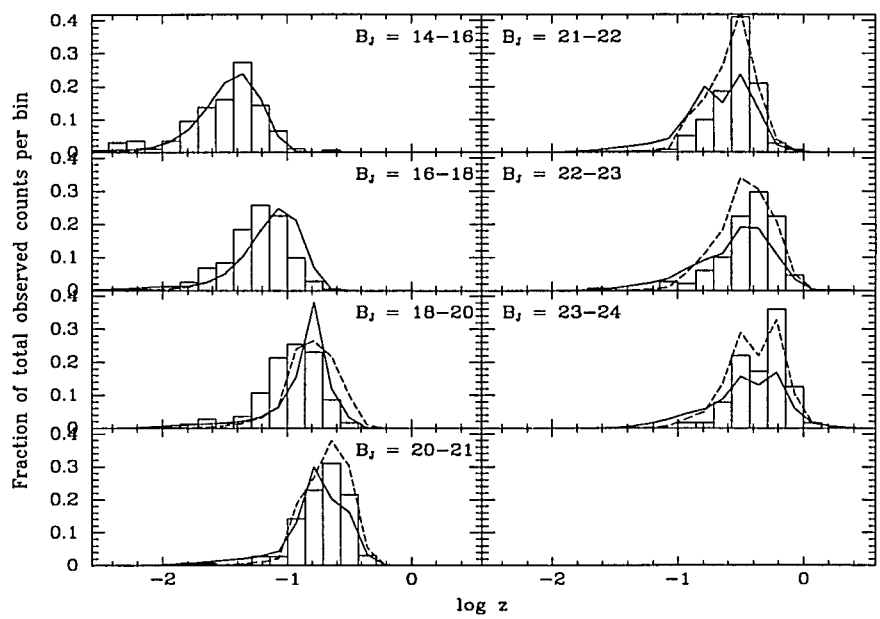

Fig. 3.8.—
Redshift distributions for burst populations. Solid line is for $0.1 - 125\ M_{\odot}$ IMF. Dashed line is for $2.5 - 125\ M_{\odot}$ IMF.

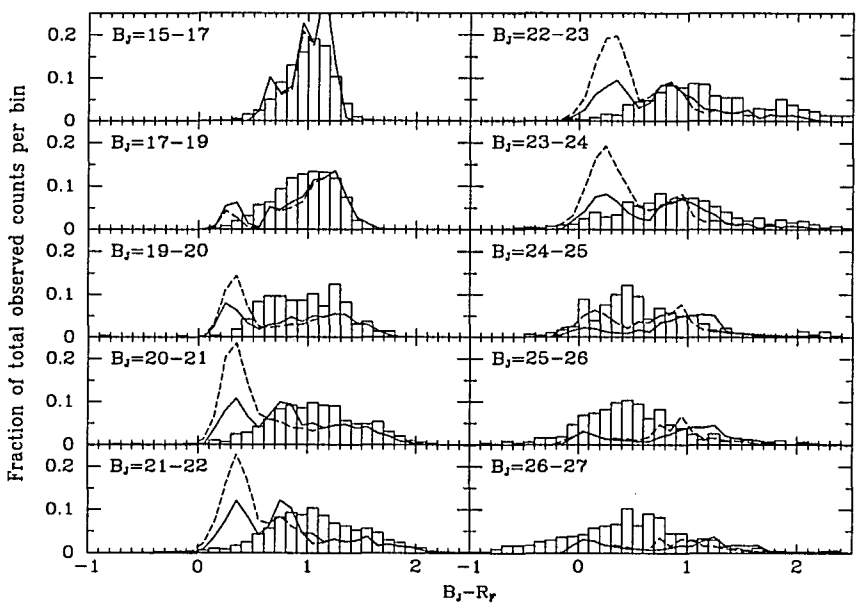

Fig. 3.9.—
B_J–R_F color distributions for burst populations. Solid line is for $0.1-125\ M_\odot$ IMF. Dashed line is for $2.5-125\ M_\odot$ IMF.

ones above, but because the burst fades so rapidly, we assume that the effective bright lifetime of the burst is the same as the burst length, 0.1 Gyr. Thus the LFs have a normalization twice as large as previously. For this IMF a $M_{B_J} = -19.0$ galaxy has a mass of $6 \times 10^7\, M_\odot$. The amount of fading ranges from 15 mag after 2 Gyr to 19 mag after 4.3 Gyr. After 5 Gyr the galaxy has faded completely because all the stars have turned into stellar remnants.

Figures 3.7–3.9 (dashed lines) show the distributions for this model. As in the previous burst model, the U counts are over predicted. The redshift distributions this time are better, having no tails at low redshift. The reason for this is clear: the galaxies, having no low-mass stars, fade completely and so are undetectable except in their burst phase.

3.6 Surface Brightness Effects

Up to now we have assumed that all galaxies of a given apparent magnitude will be detected. In practice, a galaxy will be detected only if its observed surface brightness is above a threshold value (μ_{det}) over a minimum angular area (A_{min}). The values of μ_{det} and A_{min} are different for each survey. The observed surface brightness profile depends on the intrinsic galaxy profile convolved with a point spread function. In the detection process, the image is often further convolved with a smoothing function. We use the formalism developed by Yoshii (1993) to compute the detectability of galaxies. The detected magnitude of a galaxy differs from the total integrated magnitude by $\Delta = m_{det} - m_{tot} = -2.5\log(\tilde{G}(\theta_{det})/\tilde{G}(\theta)))$, where $\tilde{G}(\theta)$ is Yoshii's notation for the integrated intensity out to radius θ. The expression for $\tilde{G}$ depends on a galaxy's intrinsic profile, its redshift, and the seeing conditions. The value of θ_{det} is fixed for an aperture magnitude, and for

an isophotal magnitude, again depends on the galaxy's properties. Thus Δ is a function of galaxy type, M, z, and the detection conditions. To compute Eq. 3.1 & 3.3 we first iteratively solve Eq. 3.2 for M, then determine whether the galaxy survives the detection criteria before evaluating the LF.

Table 3.8 lists the surface brightness selection criteria we adopt for the redshift distributions. We have tried to take from the literature the parameters used to produce the observed distributions. However, often the information given in the papers is incomplete and we have made reasonable guesses for the missing parameters. In some cases the redshifts come from several sources with different selection criteria. Thus the precise quantitative effects of the selection criteria should not be taken as absolute, but we believe that the effects shown are quite representative.

3.6.1 Quiescent population

For our quiescent population we assume that the E and S0 types have an $r^{1/4}$ profile where the central surface brightness, μ_0 at $z = 0$ is assumed to be $14.8 B_J$ mag arcsec^{-2} (Fish 1964). For the spirals we assume an exponential profile with μ_0=21.0 for types Sab and Sc, and μ_0=22.2 for Sdm and Irr (van der Kruit 1987). These are the mean apparent central surface brightnesses for these galaxy types, rather than a value corrected for inclination. This is appropriate because in our calculation we make no consideration of galaxies of different inclinations. Van der Kruit's results are fully consistent with those of Freeman (1970) who obtained μ_0=21.7 averaged over all types after inclination correction.

Table 3.8. Surface brightness selection criteria

Filter	m	FWHM ["]	μ_{det} [mag/□"]	r_{min} ["]	Magnitude Type	Source
			Criteria for $n(z)$			
B_J	14-18	1.0[a]	25.0	2.0[a]	Total	Metcalfe et al. (1989)
B_J	18-21	1.8[a]	25.5[a]	0.6[a]	Total[a]	Koo (unpublished)
B_J	21-23	1.8	26.5	0.6	Total	Colless et al. (1990)
B_J	23-24	1.1[a]	29.0	0.8[a]	3" aperture	Lilly et al. (1991)
			Criteria for $n(m)$			
B_J	< 19	1.0	24.7	1.1	Pseudototal[b]	Maddox et al. (1990b)
B_J	18-23	1.8	26.5	0.6	Isophotal	Jones et al. (1991)
B_J	22-27	1.0	29.0	0.8	Isophotal	Tyson (1988)
K	17-20	2.1	23.0	1.3	Pseudototal[c]	Chapter 2
K	19-21	1.8	23.6	0.5	3" aperture	Cowie[d]

[a]Estimated–not given in source.
[b]Used correction scheme given in Maddox et al. (1990a)
[c]Flux is measured in area double that defined by μ_{det}
[d]As presented by Yoshii (1993)

3.6.2 Burst population

For the burst population we make the same assumption with regards to central surface brightness as for the quiescent population: galaxies of the same age have the same central surface brightness for all magnitudes. Figure 3.10 shows the predicted redshift distributions for three scalings: for a $10^8 M_\odot$ burst the galaxies have half-light radii (r_e) of 1 (solid), 3 (dashed), and 10 kpc (dotted).

In the $B_J = 21 - 23$ bins, the low-redshift tails are strongly dependent on the sizes of the burst galaxies. With the normal IMF, a $10^8 M_\odot$ burst corresponds to an absolute magnitude of $M_{B_J} = -18$ during the bright phase. High-resolution imaging of a sample of galaxies with $21 < B_J < 22.5$ (Colless et al. 1994) shows that such a galaxy should have $r_e \approx 2$ kpc. This corresponds to between the dashed and solid lines of Figure 3.10, at a level where the low-redshift tails are still in conflict with the observations. It is worth noting that the effects of surface brightness selection are different in each of the redshift bins. This points out the importance of understanding the selection criteria for each survey.

3.6.3 Low surface brightness galaxies

Disk galaxies with low surface brightness (LSB) are known to exist in the local universe (McGaugh 1992) but are not included in the luminosity functions derived from large area photographic surveys (Impey 1993). A derivation of the luminosity function of these galaxies is not yet available but they are believed to exist in numbers comparable to the high surface brightness galaxies. McGaugh (1994) has argued that these LSB galaxies are identical to the faint blue galaxies that are missing from the baseline model. We now add such a population to

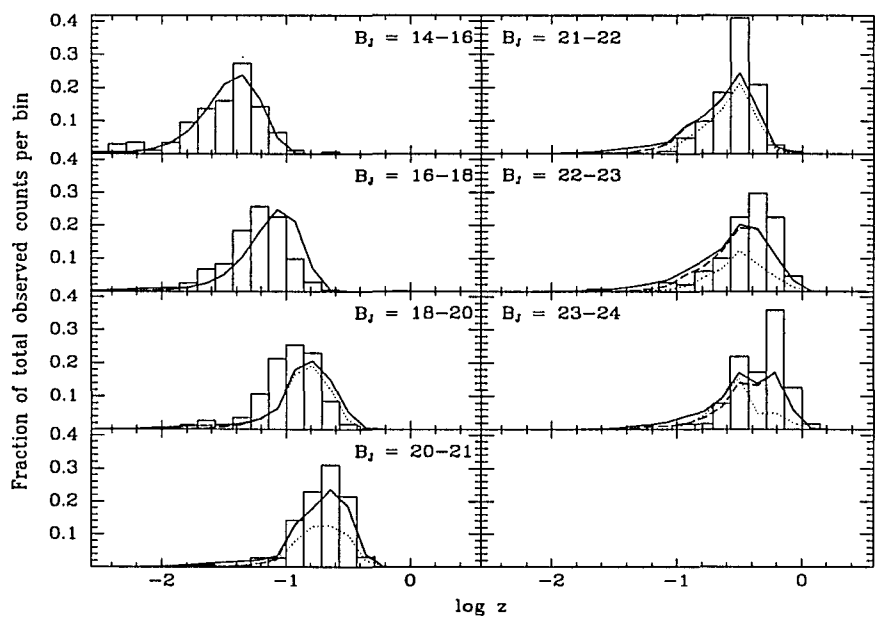

Fig. 3.10.—
B_J selected redshift distributions for the baseline plus local IMF burst populations. The solid, dashed and dotted curves are for populations where a $10^8 M_\odot$ burst has r_e = 1, 3, and 10 kpc respectively ($H_0 = 50\,\mathrm{km\,s^{-1}\,Mpc^{-1}}$, $q_0 = 0.05$) . The three curves are degenerate in the upper-left plots because the burst population does not contribute at those magnitudes.

our model. The evolutionary history of such galaxies is not well understood (McGaugh & Bothun 1994) so for simplicity we assume a single SED of constant star formation with age 5 Gyr. This SED has colors $U-B=-0.18, B-V=0.33$, and $V-I=0.96$, chosen to match the median colors of the LSB galaxies, $U-B=-0.17, B-V=0.44$, and $V-I=0.89$ (McGaugh and Bothun 1994). We will assume a single luminosity function identical to that for high surface brightness galaxies: $\phi=0.00175\,\mathrm{Mpc}^{-3}\,\mathrm{mag}^{-1}$, $\alpha=-0.97, M^*_{B_J}=-21.0$ (Loveday 1992). Additionally we assume no evolution for the LSB SED. By this we do not imply that these galaxies do not evolve, but we assume that the population as a whole does not change with time. These assumptions will certainly be subject to revision as more information on the LSB galaxy population becomes available.

Figure 3.11 shows that adding the LSB population has its strongest effect on the B_J counts between 18 and 23. The nearby galaxies are not affected greatly because the surface brightness threshold in the local survey (Maddox et al. 1990b) is too high to detect many of them. For those that are detected, the extrapolation to pseudototal magnitudes (Maddox et al. 1990a) underestimates the actual magnitude by up 1 mag. At intermediate magnitudes the increased sensitivity of the surveys allows them to be detected. However, at high redshift in the absence of evolution, the galaxies once again are too faint to detect. The known population of LSB galaxies can explain the observations only for $B_J \lesssim 23$.

3.7 K-selected colors

Galaxies selected at $K-$band are a powerful probe of higher redshifts because of the smaller KE-corrections at longer wavelengths. Figure 3.12 shows the color distributions of galaxies from the sample described in Chapter 2. Overplotted

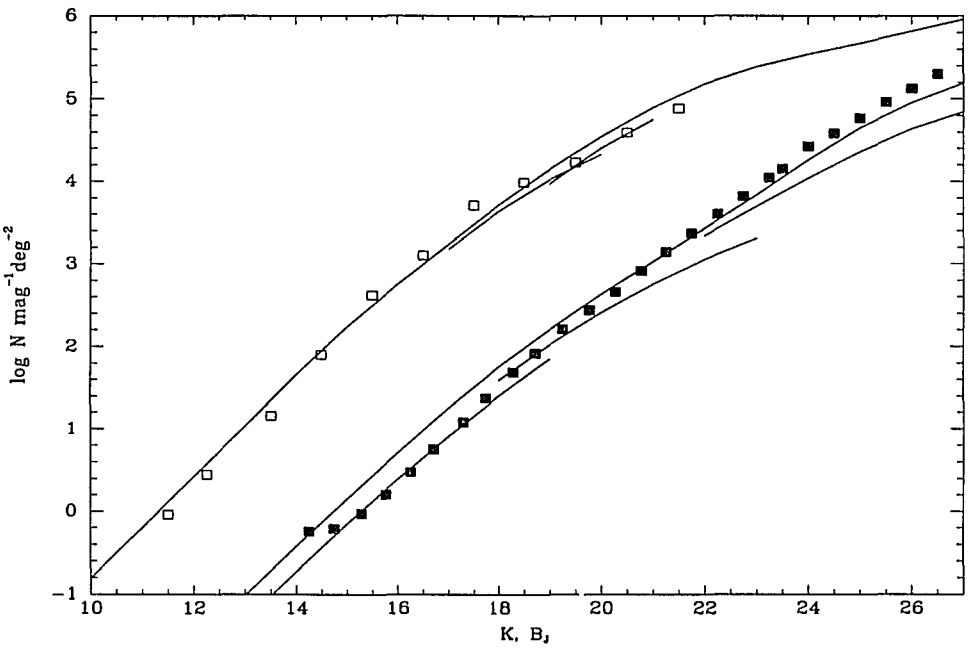

Fig. 3.11.—
Number vs. magnitude for a baseline population plus an equivalent number of LSB galaxies. The long-upper curves are for no surface brightness selection. The lower 3 curves show what should actually be observed using the selection criteria that are listed in Table 3.8. The predictions match the observations fairly well for $B_J \lesssim 23$.

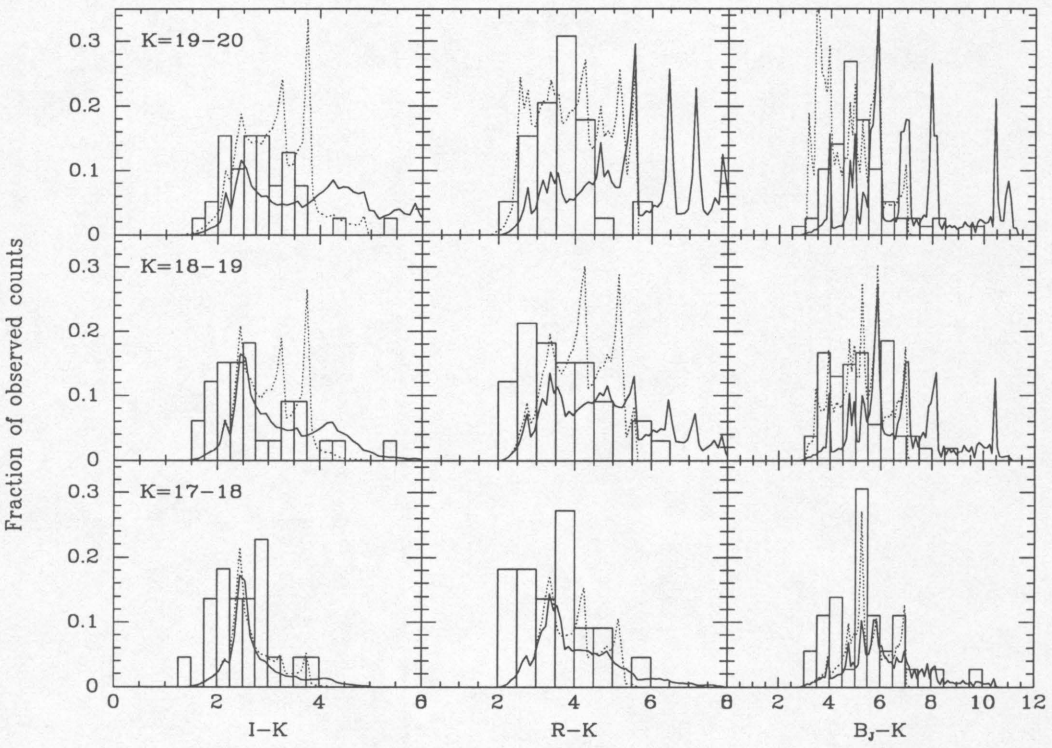

Fig. 3.12.—
Colors of K-selected galaxies. The K-magnitude range is shown in the left panel of each row. The histogra shows data from Chapter 2. Solid line is for the baseline population with constant SFR. Dotted line is for the modified population with exponential SFR.

(solid lines) is the predicted distribution from the baseline population. It is immediately clear that in the $K = 19 - 20$ range, the model predicts colors that are too red. From Figure 3.13 we see that the predicted red galaxies are high-redshift objects with low amounts of star formation. The spikes in the $R - K$ and $B_J - K$ distributions are caused by the fact the model contains a discrete number of galaxy types and the color curves are flat at high redshift. In reality these distributions will be smoothed out. A particularly important color to consider is $I - K$ because even at redshifts approaching 2, the observed I band is still emitted longward of 3000Å where we have fairly good knowledge of what the SEDs look like. The blue colors of the galaxies suggest two possibilities. The first is that the galaxies in the $K = 19 - 20$ range are not at such high redshift. This would be the case if significant numbers of galaxy mergers occurred since redshift $1 - 2$ and we are seeing the galaxies before merging.

The second possibility is that the star-formation rate of present-day red galaxies was significantly higher at $z \approx 1$. We now replace the E and S0 populations from the baseline model with an exponentially decaying star-formation rate SED with $\tau = 1$Gyr. The Sab SED is replaced with $\tau = 2$Gyr. For comparison with Table 3.6 these SEDs have present day (age = 13.5 Gyr) $B - V$ colors of 0.91 and 0.87 respectively. At $z = 1.5$ the observed colors are considerably bluer than their constant-SFR counterparts with $I - K = 3.8$ and 3.25 respectively. The dotted curves in Figure 3.12 show a better agreement with the observations than the baseline model. However, the B_J redshift distributions now predict too many high-redshift galaxies compared with the observations (Figure 3.14).

The definitive test to distinguish between merging and an increased SFR requires determining redshifts for K-selected galaxies. Elston (1994) has reported results of a redshift survey of galaxies with $K < 18$ and $R < 22$ that shows a

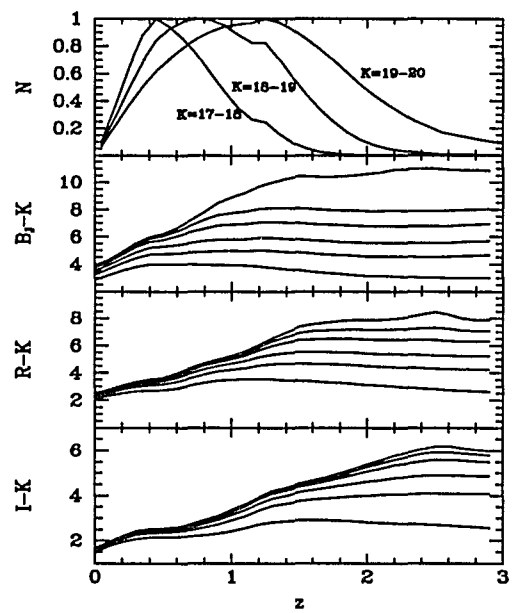

Fig. 3.13.—
The bottom three panels show the colors of the evolving baseline population as a function of redshift. The six curves are for the E though Im types from top to bottom. The upper panel shows the predicted redshift distributions for a $K-$selected population. From left to right the three curves are for $K = 17-18$, $18-19$ and $19-20$.

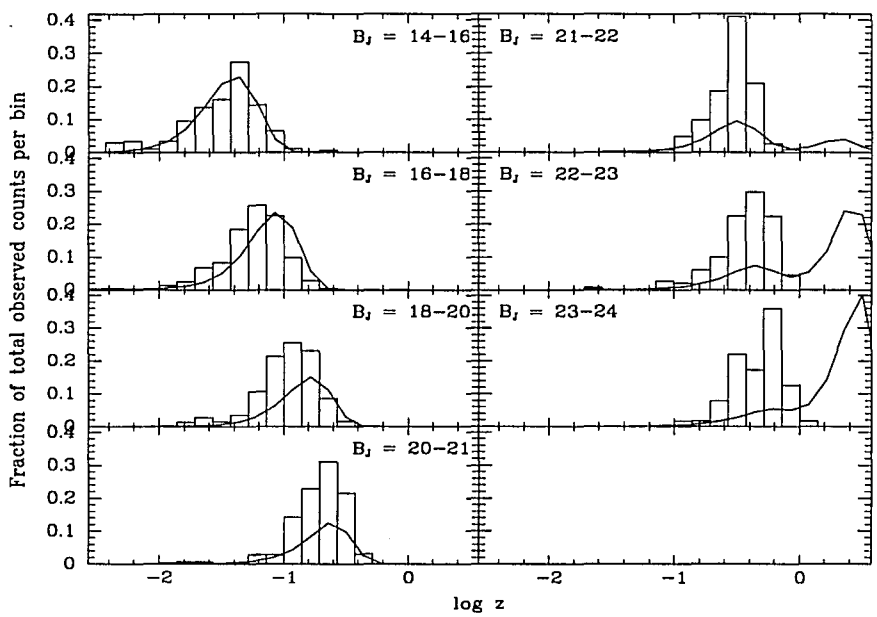

Fig. 3.14.—
B_J-selected redshift distributions for the modified baseline population. The increased evolution of the red galaxies adds too many galaxies in the blue. For this model to work, dust must extinguish the blue light.

median redshift > 0.5, implying that mergers are relatively unimportant at low redshift. In contrast, a partially complete survey to $K = 20$ (Songaila et al. 1994) shows that the majority of galaxies are not at high redshift. Additional surveys to K =19–20 are currently underway in the UK and Arizona. The discrepancy between the baseline model and the observations becomes most apparent in the $K = 19 - 20$ range, but determining complete samples of redshifts here will be quite difficult as a majority of the galaxies have $B_J > 24$. The high-redshift galaxies, unfortunately, will be the most difficult to get redshifts for as the k-correction makes them the reddest.

3.8 Summary

We have explored several scenarios for explaining the magnitude, redshift and color distributions of galaxies. The baseline population of galaxies consists of an initial burst of star formation, followed by constant star formation thereafter. We conclude

1. The baseline population with passive evolution underestimates the slope of number vs. magnitude at B_J.

2. Adding a population of starburst galaxies to increase the counts at B_J adds too many low-redshift remnants not seen in the z distributions. The starbursts do not fade enough to be absent from local surveys.

3. Changing the IMF of the burst population removes the low-redshift tail problem. Both starburst populations produce galaxies that are too blue in $B_J - R_F$.

4. Adding surface brightness selection to the simulation has significant effects on the $n(m)$ and $n(z)$ relations at all magnitudes. The low-z tails produced by the local IMF starburst population are diminished but not eliminated.

5. Adding a population of low surface brightness galaxies, which are known to exist locally, removes much of the discrepancy in the counts brighter than $B_J = 23$. At fainter magnitudes there is still a problem. Full understanding of this effect will require LFs corrected for surface brightness effects.

6. The blue $I - K$ colors of galaxies selected with $K = 19 - 20$ show that an old quiescent population is not an adequate model for elliptical galaxies. Making the galaxies bluer can be accomplished by having them at z=1 but forming more stars. This appears to be ruled out by the B_J selected redshift distributions. The alternative is to increase the number of lower redshift galaxies. They are bluer because of the k-corrections. The physical mechanism to accomplish this is not clear, though one possibility is for these galaxies to be in a premerged state.

New observational results can provide constraints to some of these issues. A determination of the local LF as a function of spectral type and surface brightness will allow a better determination of the baseline population. Multicolor digital sky surveys (e.g. Gunn & Knapp 1993) should explain some of the discrepancies in the bright-end counts. Finally, expanded K-band selected redshift surveys will provide information on the amount of merging since z=1.

Chapter 4

MG RADIO GALAXIES

In this chapter we consider a sample of radio-selected galaxies with lower radio power than those in the 3CR catalog. They will be used to investigate the relation of radio power to absolute K magnitude and color.

4.1 Sample Definition

Over 3000 sources with $S_\nu(5\,\mathrm{GHz}) > 100\,\mathrm{mJy}$ from the MIT - Green Bank radio survey (MG-I)(Bennett et al. 1986) have been imaged at the Very Large Array telescope by B. Burke and S. Conner (Dickinson, private communication). Spinrad et al. (1993) are obtaining optical identifications and redshifts for those sources with angular size smaller than $10''$ and spectral index $\alpha > 0.75$. The size restriction eliminates low-redshift objects. The spectral index, measured between 1.4 and 5 GHz, where $S_\nu \propto \nu^{-\alpha}$, is used to eliminate many objects which are likely to be quasars. This is useful because although quasars may have either flat or steep spectra, very few galaxies have flat spectra. At the time this sample was defined in

1992 November there were 60 of the 216 objects with redshifts, 47 of which were classified as galaxies, based on spectra and morphology. We have imaged 25 of the 28 galaxies with $0.83 < z < 2.00$. The missing three were omitted purely for weather or scheduling reasons.

4.2 Observations and Reductions

4.2.1 Infrared

We have obtained J, H, and K_s (hereafter just K) images using the 128×128 NICMOS2 camera at the MMT. The observing and data reduction procedures are the same as those described in Chapter 2. The images were obtained in six observing runs between 1992 February and 1993 May. We were able to get images of all 25 galaxies at H and K, and 18 at J. Typical total integration times were 60 minutes per filter per galaxy. The seeing ranged from 0.″8 to 1.″4 FWHM with a median of 1.″08 and a 1-σ scatter of 0.″14. The lower limit is almost certainly an overestimate of the true seeing because it became less than two pixels. When possible, the individual 60sec exposures were registered to the nearest integer pixel using bright objects in the frames. In those images where there were no suitable objects, the offsets sent to the telescope mount were used to shift the images. A comparison of the two techniques shows that doing the blind shifting degrades the image FWHM typically by only 0.″1. Table 4.1 lists all of the observations.

As with the deep images of Chapter 2 the photometry was done relative to the stars we used to stack the six MMT images. One second long images of these "stack" stars were obtained every three minutes as part of the observing procedure. These stars provide a measure of both the photometric stability and of the point

Table 4.1. Log of observations

Galaxy Name (1950)	Filter	UT Date	Integration sec	Seeing arcsec
0019 + 110	H	92 Oct 9	1350	1.07
	Ks	92 Oct 12	880	1.08
0023 + 132	B	92 Oct 26	1800	1.36
	R	92 Oct 26	2400	1.28
	H	92 Oct 11	825	1.42
	Ks	92 Oct 12	780	1.07
0023 + 171	H	92 Oct 11	920	1.06
	Ks	92 Oct 12	1080	1.01
0049 + 117	B	92 Oct 26	1800	1.23
	R	92 Oct 26	1800	1.10
	H	92 Oct 10	1650	1.12
	Ks	92 Oct 10	900	1.00
0216 + 027	B	92 Oct 26	1200	1.47
	R	92 Oct 26	1800	1.20
	J	92 Oct 12	1350	1.28
	H	92 Oct 12	1800	1.27
	Ks	92 Oct 10	2055	1.09
0717 + 150	B	94 May 3	3600	1.75
	R	92 Oct 26	3000	1.47
	J	92 Oct 10	1770	1.05
	H	92 Oct 12	930	1.08
	K	92 Feb 24	750	1.42
0738 + 157	R	92 Oct 26	3600	1.32
	H	92 Oct 9	675	1.13
	Ks	92 Oct 11	700	1.12
0852 + 029	R	92 Oct 26	1800	1.40
	J	93 Apr 12	4500	0.83
	H	93 Apr 10	720	1.17
	Ks	93 Apr 11	1380	1.16
0949 + 002	R	93 Apr 21	2400	1.29
	J	93 Apr 9	3000	1.21
	H	93 Apr 10	1200	1.05
	Ks	93 Apr 9	1240	1.20
1005 + 077	H	93 May 9	1040	1.09
	Ks	93 May 8	780	1.11

Table 4.1–Continued

Galaxy	Filter	UT Date	Integration sec	Seeing arcsec
1015 + 188	B	93 May 18	2400	2.09
	J	93 May 10	3600	1.05
	H	93 May 7	1200	0.97
	Ks	93 May 9	900	1.09
1054 + 073	B	93 Apr 21	3000	1.46
	R	93 Apr 21	2400	1.28
	H	93 Apr 12	920	0.89
	Ks	93 Apr 11	1200	0.91
1133 + 140	B	93 Apr 21	3600	1.39
	J	93 Apr 9	3540	1.24
	H	93 Apr 10	1020	1.17
	Ks	93 Apr 11	1100	0.93
1424 + 096	J	93 Apr 12	3600	0.94
	H	93 Apr 10	1200	1.03
	Ks	93 Apr 9	1160	1.07
1500 − 023	B	93 Apr 21	3600	1.63
	J	93 May 7	3600	1.26
	H	93 Apr 10	1160	0.99
	Ks	93 Apr 11	1200	0.83
1523 + 161	B	93 Apr 22	3000	1.26
	J	93 May 8	3600	1.05
	H	93 Apr 12	1160	0.91
	Ks	93 Apr 12	1120	0.85
1557 + 164	R	93 Apr 21	3000	1.44
	J	93 May 9	3600	0.86
	H	93 Apr 10	1200	1.03
	Js	93 Apr 9	1200	1.01
1638 + 132	B	93 May 19	3600	1.71
	R	93 May 19	2400	1.54
	J	93 May 10	3600	0.95
	H	92 Apr 12	3060	1.05
	Ks	93 May 8	1200	1.11
1701 + 051	J	93 Apr 11	3600	0.88
	H	93 Apr 10	1080	0.99
	Ks	93 Apr 9	1340	1.21

Table 4.1–Continued

Galaxy	Filter	UT Date	Integration sec	Seeing arcsec
1714 + 023	B	93 May 19	3000	1.64
	J	93 May 10	3600	0.84
	H	92 Apr 13	1680	1.12
	Ks	93 May 9	1200	0.79
1714 + 060	J	93 Apr 11	2100	0.82
	H	93 May 9	1200	1.05
	Ks	93 May 8	900	1.15
1742 + 166	B	93 Apr 22	3600	1.45
	R	92 Apr 22	2400	1.16
	J	93 May 10	3600	0.88
	H	92 Oct 12	765	1.23
	Ks	92 Oct 11	720	1.25
1824 + 092	B	93 Apr 21	3600	1.68
	R	92 Apr 22	2400	1.11
	J	93 May 7	2520	1.18
	H	92 Oct 10	675	1.21
	Ks	93 May 9	600	0.81
2108 + 039	B	92 May 19	2400	2.16
	J	92 Oct 10	1350	1.20
	H	92 Oct 10	1350	1.15
	Ks	92 Oct 11	560	1.16
2300 + 134	R	92 Oct 26	1800	1.39
	J	92 Oct 11	1350	1.04
	H	92 Oct 12	1440	1.22
	Ks	92 Oct 10	1770	1.21

spread function during each galaxy observation. Photometry of these stars was obtained at the Catalina 1.55m telescope on two nights: 1992 Oct 2 and 1993 Feb 3 UT. One-sigma residuals on the first night were 0.05 mag and on the second, 0.03 mag. Table 4.2 lists the HST Guide Star catalog numbers and derived IR photometry for the observed stack stars. The photometry was referenced to the standards of Elias et al. (1982).

4.2.2 Visible

We also have CCD images obtained with the Steward Observatory Kitt Peak 2.3m telescope through B and R filters onto the 1200 × 800 pixel Loral CCD. We were able to obtain images of 14 galaxies at B and 12 at R over the nights of 1992 October 26 UT, 1993 April 21-22, 1993 May 19, and 1994 Mar 3. Typically 4-6 600 sec exposures were obtained of each galaxy with each filter. The numerous cosmic ray hits were edited out of the immediate neighborhood of the galaxy by hand using the IRAF[1] "imedit" task, and the images were averaged with no further pixel rejection. Experimentation showed that using rejection algorithms when combining the images to remove the cosmic rays resulted in photometric errors of several percent being introduced on the stellar images in the frames. This was due to faulty pixel rejection in the centers of the bright stars where the intensity could vary from frame to frame as the registration and seeing changed slightly. Magnitude zero-points were determined using the standards of Landolt (1983;1992), Christian et al. (1985), and Odewahn, Bryja, & Humphreys (1993).

---

[1]Image Reduction and Analysis Facility software, National Optical Astronomy Observatories

Table 4.2. Stack star photometry

Galaxy	StarName	J	H	Ks	Notes
0019+110	0599/0907	9.92	9.64	9.54	1
0023+132	0602/0525	8.53	7.95	7.78	1
0023+171	1180/0040	10.22	9.77	9.65	1
0216+027	0041/1627	9.58	9.33	9.26	1
0717+150	0775/1602	9.12	9.18	9.23	1
0738+157	1361/2758	9.48	8.93	8.80	1
0852+029	0217/0978	11.15	10.83	10.80	1
0949+002	4896/1331	10.50	10.10	10.01	2
1015+188	1422/0751	9.51	9.17	9.08	2
1054+073	0261/0198	10.90	10.54	10.47	2
1424+096	0909/0499	11.65	11.36	11.33	2
1500−023	5004/0470	11.05	10.59	10.48	2
1523+161	1487/0956	10.54	10.18	10.11	2
1557+164	1496/1189	10.55	9.98	9.84	2
1638+132	0969/0960	11.72	11.25	11.15	1
1714+023	0404/1455	10.30	9.81	9.65	1
1742+166	1552/0686	9.53	8.98	8.85	1
1824+092	1023/0254	10.64	10.37	10.30	1
2119+184	1667/0079	8.08	7.34	6.96	1
2300+134	1166/1393	10.78	10.54	10.42	1

Note. — 1: Observed 1993 March, $\sigma \approx 0.03$ mag.
2: Observed 1992 October, $\sigma \approx 0.05$ mag.

4.3 Results

Figure 4.1 shows $28'' \times 28''$ regions surrounding each of the galaxies. In each case the image is centered on the nominal radio coordinates of the galaxy as offset from the HST guide star used for stacking.

Photometry on each galaxy was measured in two apertures, with diameters $4''$ and $8''$. A local sky level was determined in a 5 pixel wide annulus at a radius of $12''$. Errors on the photometry were determined by measuring the sigma of the sky pixels and scaling appropriately to the size of aperture. Aperture corrections were determined for each image by measuring the fraction of light within each aperture for bright stellar images. For the IR images this was done with the stack-star images. Thus the aperture magnitudes properly account for light spilled over the aperture due to seeing, but do not try to correct for the fact that the galaxy may extend beyond the aperture. Photometry for all the galaxies is listed in Table 4.3. Galactic reddening values (Burstein & Heiles 1982) are also shown. Extinction corrections are not applied to the values in the table but are applied in the spectral energy distribution (SED) analysis below. In several cases, neighboring galaxies fell in the larger apertures. These cases are flagged in the table.

4.3.1 Spectral Energy Distributions

For all the galaxies in the sample which have a measured B or R mag we have fit composite SEDs to the broadband fluxes. The fit SEDs consist of two standard components, red and blue. The red component is a 10 Gyr old stellar population that began with a 1 Gyr long star-formation period (Bruzual & Charlot 1993). The blue component is a power law of the form $F_\nu \propto \nu^{-0.2}$ (Dunlop & Peacock 1993).

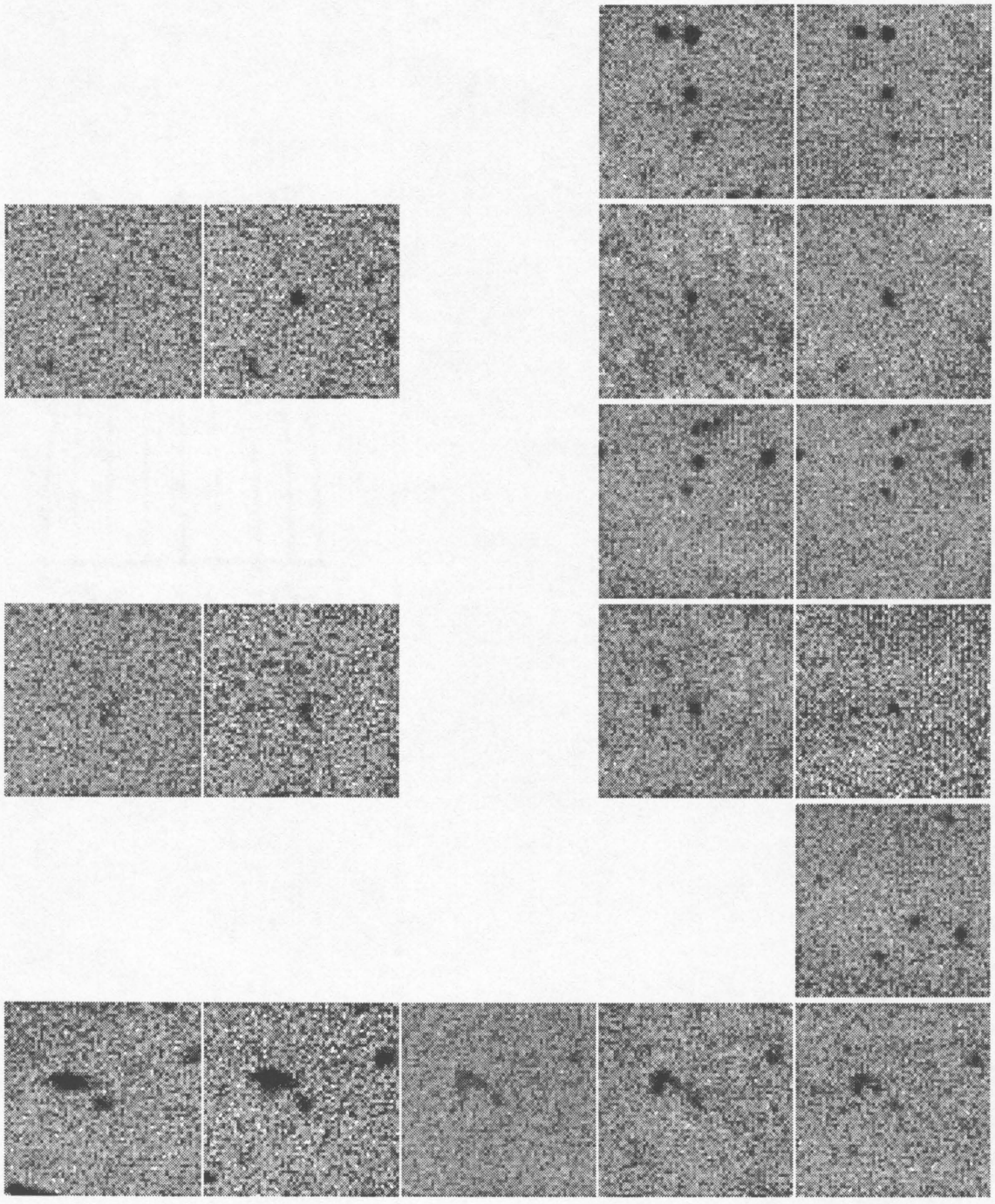

Fig. 4.1.—
Images of MG radio galaxies. North is up and east is to the left. From left to right the bandpasses are B, R, J, H, and K. From top to bottom the galaxies are 0019+110, 0023+132, 0023+171, 0049+117, 0109+1839 (z=1.26, but not in originally defined sample), and 0216+027.

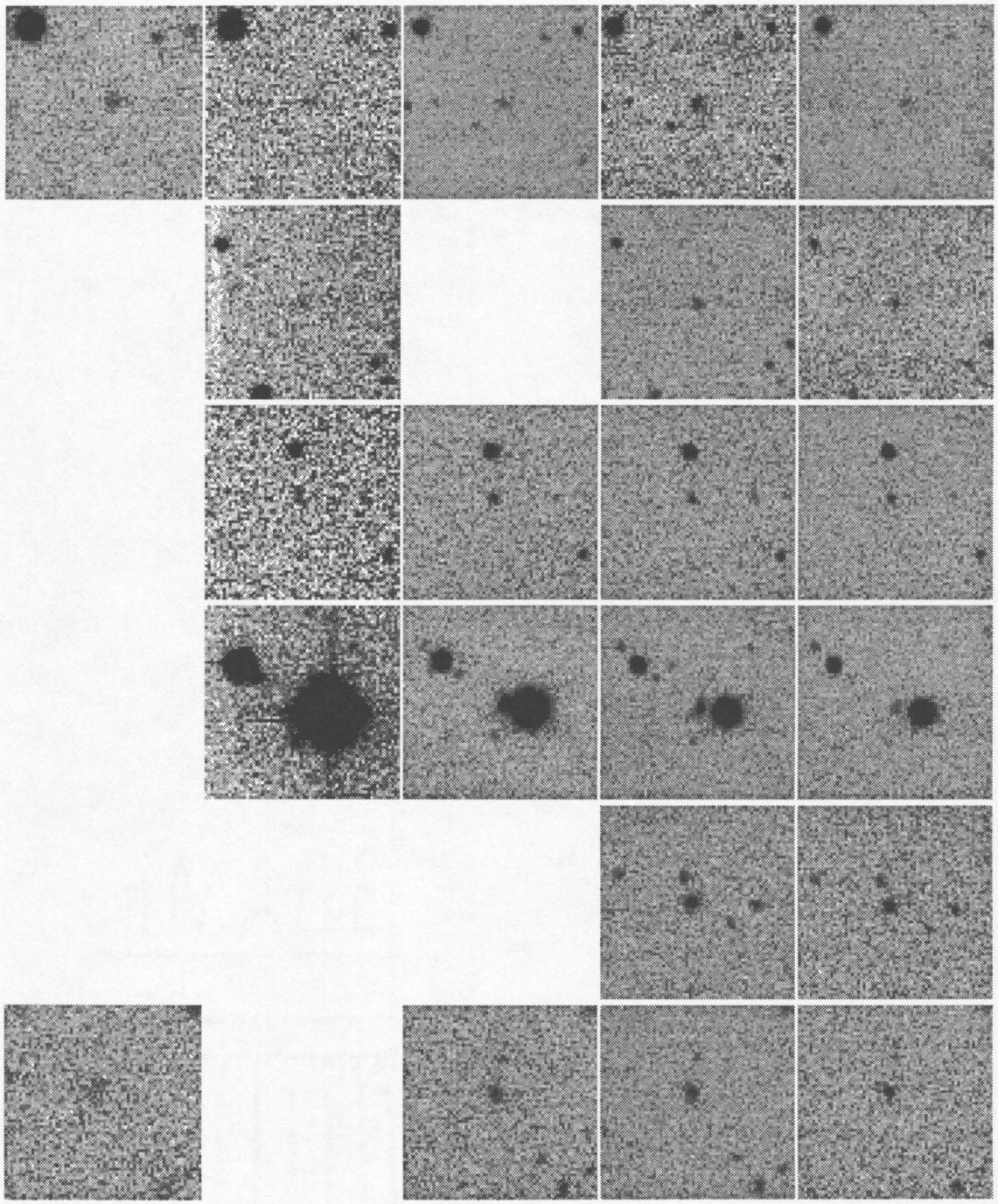

Fig. 4.1–continued. From top to bottom the galaxies are 0717+150, 0783+157, 0852+029, 0949+002, 1005+077, and 1015+188.

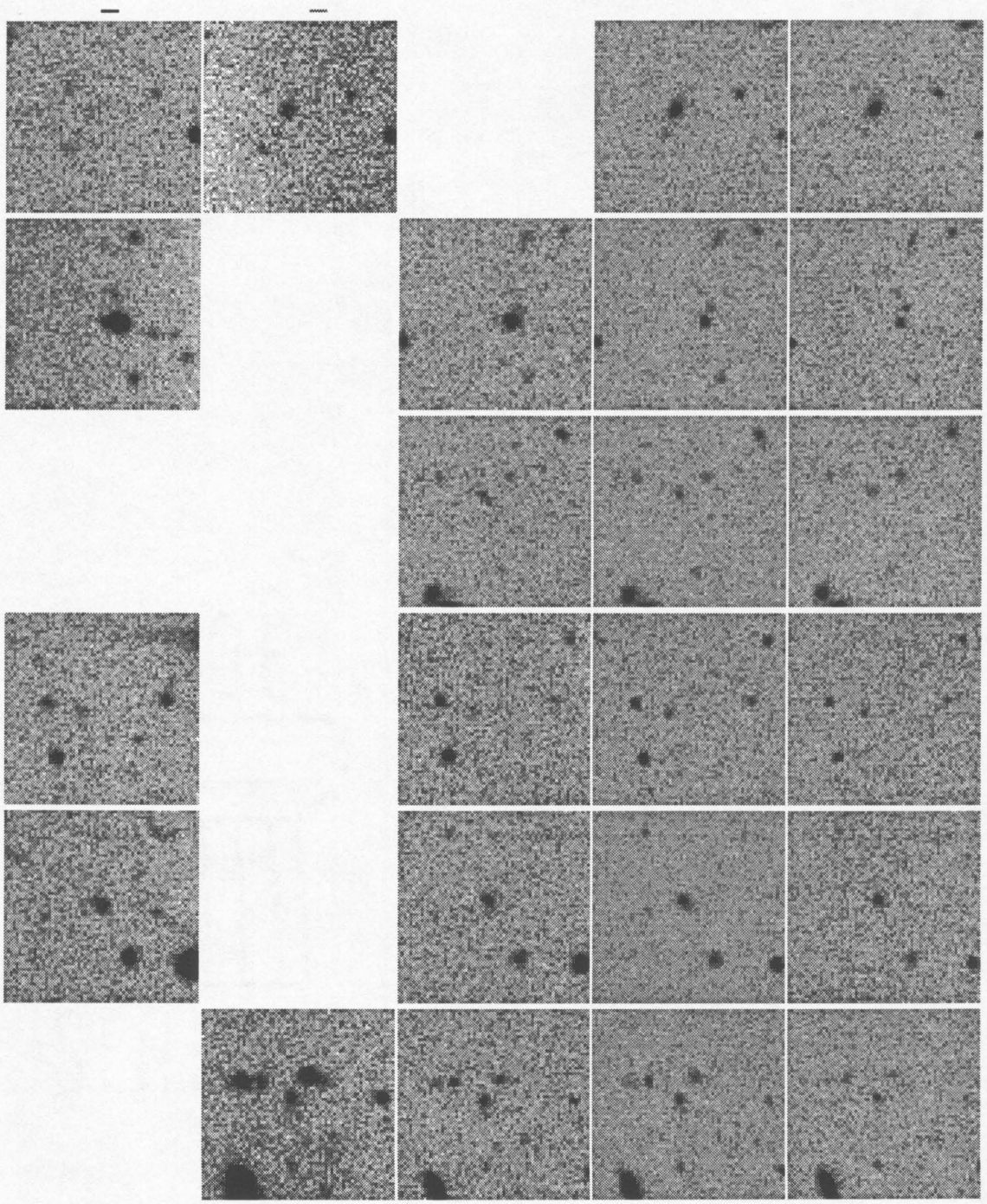

Fig. 4.1–continued. From top to bottom the galaxies are 1054+073, 1133+140, 1424+096, 1500−023, 1523+161, and 1557+164.

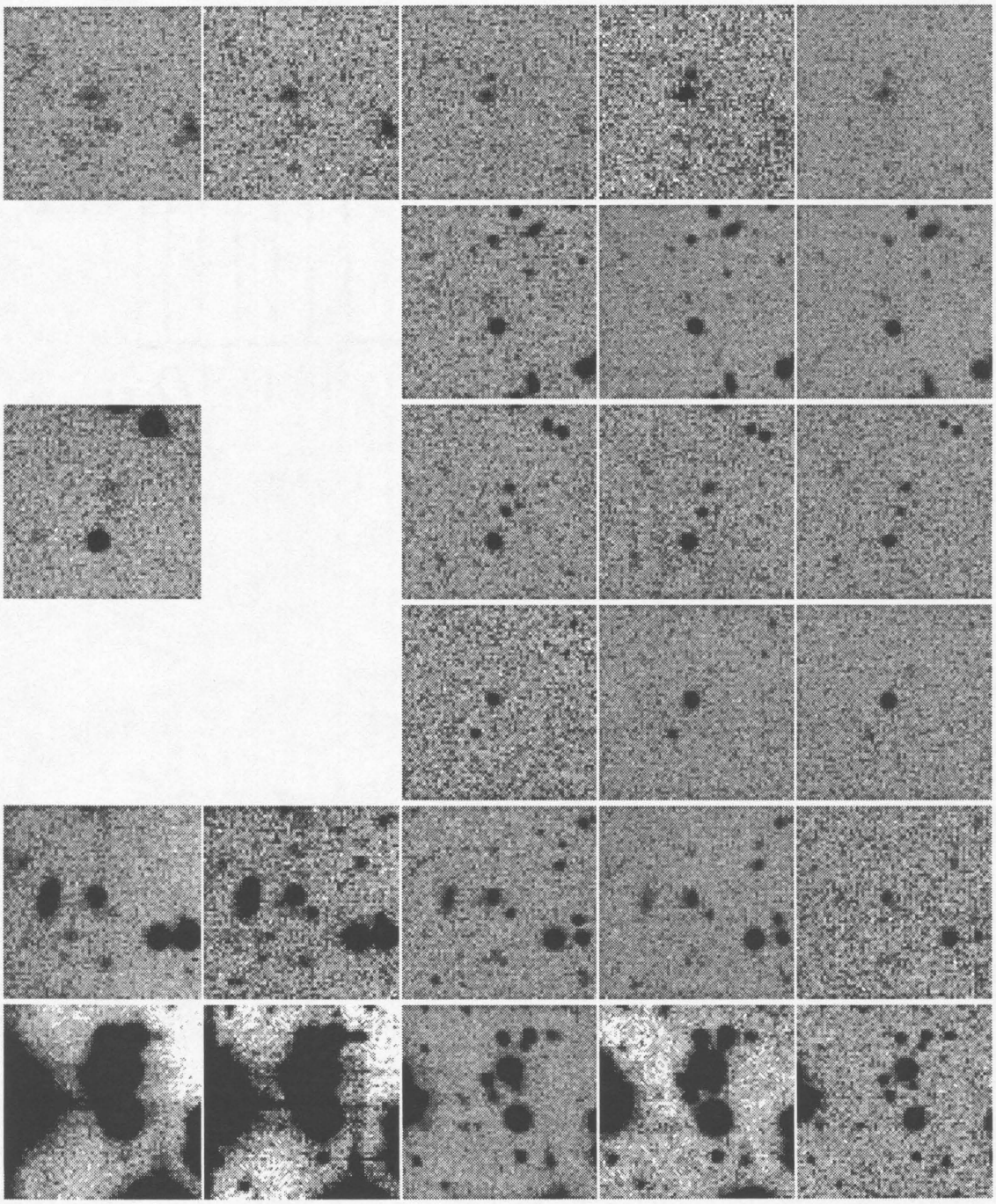

Fig. 4.1–continued. From top to bottom the galaxies are 1638+132, 1701+051, 1714+023, 1714+060, 1742+166, and 1842+092.

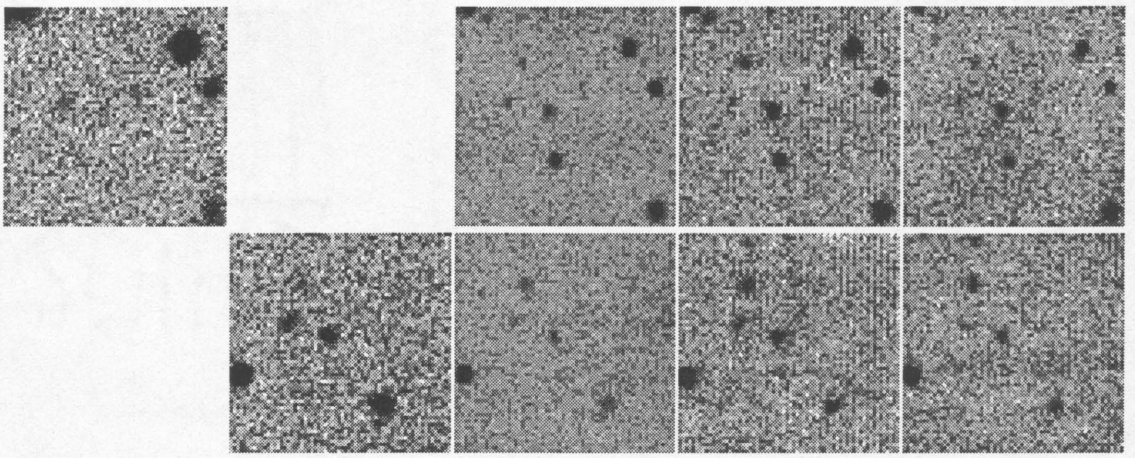

Fig. 4.1–continued. From top to bottom the galaxies are 2108+039 and 2300+134.

This component represents recent star formation and/or blue light from an AGN. The ratio of the amplitudes of the blue and red components is defined by their relative fluxes at rest wavelength 5000Å, denoted f_{5000} (Lilly 1989).

The results of the fits and the observed data points are shown in Figure 4.2. For those galaxies with no CCD observations, the observed data are shown with no fit. For the vast majority of the galaxies, the data are fit by the two-component model quite well. This implies that the IR flux is dominated by light from old stars. There are three galaxies with noticeable residuals in the IR colors: 1133+140, 1824+092, and 2300+134. These are also the three galaxies with the largest values of f_{5000}. In each of these cases, a large H-α equivalent width can account for the unusual colors. These are most likely broad-line radio galaxies, which often have very bright nuclei. One of them, 1133+140, is only marginally resolved and probably is dominated by nuclear emission at all wavelengths.

We now consider the correlation of f_{5000} with radio power. If the blue component results from the same source of energy as the radio emission, then a correlation might be expected. Previous results have been conflicting on the

Table 4.3. Galaxy photometry

Galaxy	z	E($B-V$)	$B(4'')$ $B(8'')$	$R(4'')$ $R(8'')$	$J(4'')$ $J(8'')$	$H(4'')$ $H(8'')$	$K(4'')$ $K(8'')$
0019+110	1.040	0.042				18.40 ± 0.05	17.55 ± 0.07
						18.22 ± 0.10	17.47 ± 0.14
0023+132	0.900	0.034	23.90 ± 0.18	21.84 ± 0.06		18.31 ± 0.08	17.28 ± 0.05
			23.75 ± 0.32	21.75 ± 0.13		17.99 ± 0.13	17.29 ± 0.12
0023+171	0.946	0.036				20.18 ± 0.32	18.45 ± 0.13
						a	18.41 ± 0.25
0049+117	0.835	0.043	23.76 ± 0.12	22.28 ± 0.09		18.85 ± 0.07	18.20 ± 0.14
			23.13 ± 0.14	21.91 ± 0.15		18.51 ± 0.11	17.93 ± 0.21
0216+027	1.680	0.028	23.15 ± 0.09	22.52 ± 0.11	20.07 ± 0.20	19.25 ± 0.10	19.10 ± 0.20
			22.98 ± 0.17^b	22.27 ± 0.20^b	19.04 ± 0.17^b	18.90 ± 0.15^b	18.42 ± 0.21^b
0717+150	1.755	0.133	24.09 ± 0.09	23.35 ± 0.28	20.00 ± 0.12	19.03 ± 0.10	18.35 ± 0.13
			24.30 ± 0.22	23.68 ± 0.77	20.28 ± 0.31	19.03 ± 0.20	18.27 ± 0.23
0738+157	1.150	0.031		23.05 ± 0.19		19.26 ± 0.12	18.37 ± 0.13
				22.64 ± 0.27		19.03 ± 0.21	18.40 ± 0.27
0852+029	1.080	0.024		22.69 ± 0.18	20.14 ± 0.10	19.54 ± 0.14	18.09 ± 0.08
				22.50 ± 0.32	19.98 ± 0.19	20.18 ± 0.51	17.69 ± 0.12
0949+002	1.480	0.020			18.77 ± 0.17	18.21 ± 0.04	18.20 ± 0.10
					c	c	c
1005+077	0.877	0.000				17.95 ± 0.04	17.14 ± 0.05
						17.63 ± 0.08^b	16.84 ± 0.09^b
1015+188	1.250	0.019	23.48 ± 0.08		19.51 ± 0.08	18.47 ± 0.05	17.63 ± 0.07
			23.13 ± 0.12		19.20 ± 0.13	18.23 ± 0.09	17.50 ± 0.13
1054+073	0.970	0.013	24.63 ± 0.18	22.14 ± 0.06		17.70 ± 0.03	16.74 ± 0.02
			24.14 ± 0.24	21.71 ± 0.10		17.45 ± 0.06	16.45 ± 0.06
1133+140	1.000	0.013	21.18 ± 0.00		18.33 ± 0.02	18.26 ± 0.04	17.55 ± 0.06
			21.12 ± 0.05		18.30 ± 0.06	18.12 ± 0.09^b	17.44 ± 0.12^b
1424+096	1.590	0.012			20.02 ± 0.09	19.32 ± 0.09	18.91 ± 0.16
					19.43 ± 0.11	18.99 ± 0.14	18.69 ± 0.27
1500-023	1.100	0.053	24.57 ± 0.16		20.67 ± 0.25	19.80 ± 0.17	18.90 ± 0.20
			25.19 ± 0.58		20.77 ± 0.53	19.68 ± 0.30	20.00 ± 1.09
1523+161	1.110	0.026	23.32 ± 0.04		19.35 ± 0.05	18.48 ± 0.04	17.45 ± 0.05
			23.12 ± 0.09		19.31 ± 0.11	18.31 ± 0.08	17.41 ± 0.11
1557+164	1.460	0.017		22.37 ± 0.06	19.62 ± 0.07	19.04 ± 0.07	18.35 ± 0.10
				21.57 ± 0.08^b	19.36 ± 0.12^b	18.80 ± 0.12^b	18.09 ± 0.16^b
1638+132	1.290	0.052	23.42 ± 0.05	22.36 ± 0.07	19.63 ± 0.07	18.49 ± 0.05	17.63 ± 0.05
			23.04 ± 0.09	22.11 ± 0.12	19.11 ± 0.10^b	18.08 ± 0.08^b	17.08 ± 0.07^b
1701+051	1.920	0.068			20.54 ± 0.18	19.86 ± 0.17	18.73 ± 0.14
					19.26 ± 0.13^b	17.99 ± 0.08^b	17.78 ± 0.12^b
1714+023	1.270	0.117	24.11 ± 0.12		19.93 ± 0.09	18.74 ± 0.09	17.93 ± 0.09
			23.84 ± 0.19		18.99 ± 0.09^b	18.16 ± 0.11^b	17.58 ± 0.13^b
1714+060	1.710	0.083			18.46 ± 0.04	16.86 ± 0.01	16.09 ± 0.01
					18.50 ± 0.09	16.81 ± 0.06	16.12 ± 0.06
1742+166	0.850	0.081	21.77 ± 0.01	20.52 ± 0.01	18.38 ± 0.02	17.63 ± 0.03	16.89 ± 0.09
			21.72 ± 0.06	20.31 ± 0.06	18.12 ± 0.06^b	17.47 ± 0.07^b	16.78 ± 0.16^b
1824+092	0.930	0.270	22.69 ± 0.20	21.36 ± 0.20	18.50 ± 0.05^d	18.46 ± 0.07^d	17.41 ± 0.08^d
			c	c	18.47 ± 0.10^d	18.28 ± 0.13^d	17.34 ± 0.16^d
2108+039	1.316	0.070	24.79 ± 0.45		19.70 ± 0.10	18.56 ± 0.06	17.56 ± 0.07
			26.14 ± 2.73		21.15 ± 0.77	18.79 ± 0.15	16.89 ± 0.09
2300+134	1.670	0.037		21.88 ± 0.07	19.99 ± 0.14	18.75 ± 0.07	18.59 ± 0.14
				21.82 ± 0.14	20.18 ± 0.36	18.59 ± 0.13	19.17 ± 0.48

Note. — a) Negative flux measured. b) Nearby companions in aperture. c) Nearby bright star prevents measurement. d) Subtracted out nearby stars with DAOPHOT before measuring.

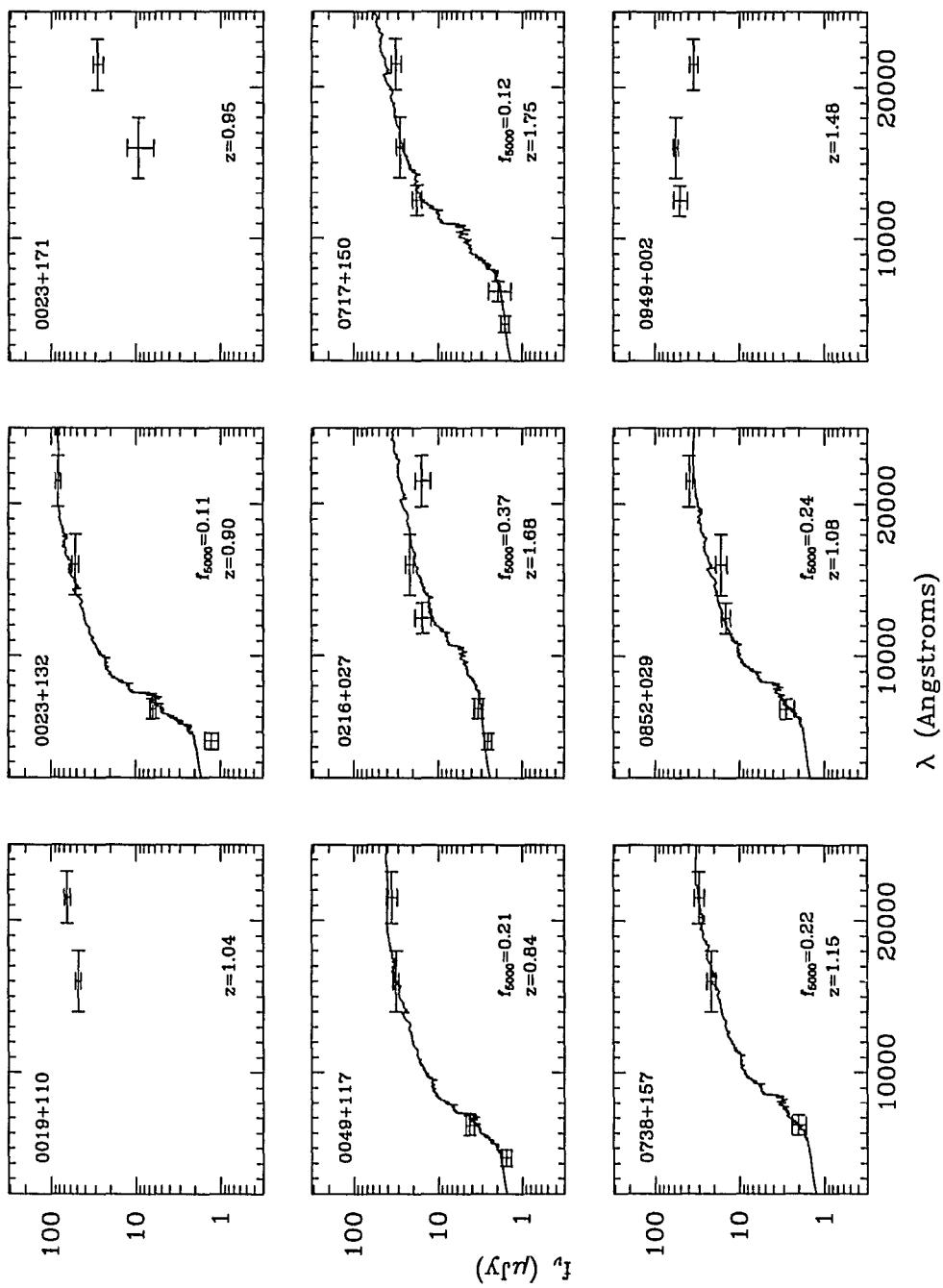

Fig. 4.2.— Spectral energy distributions

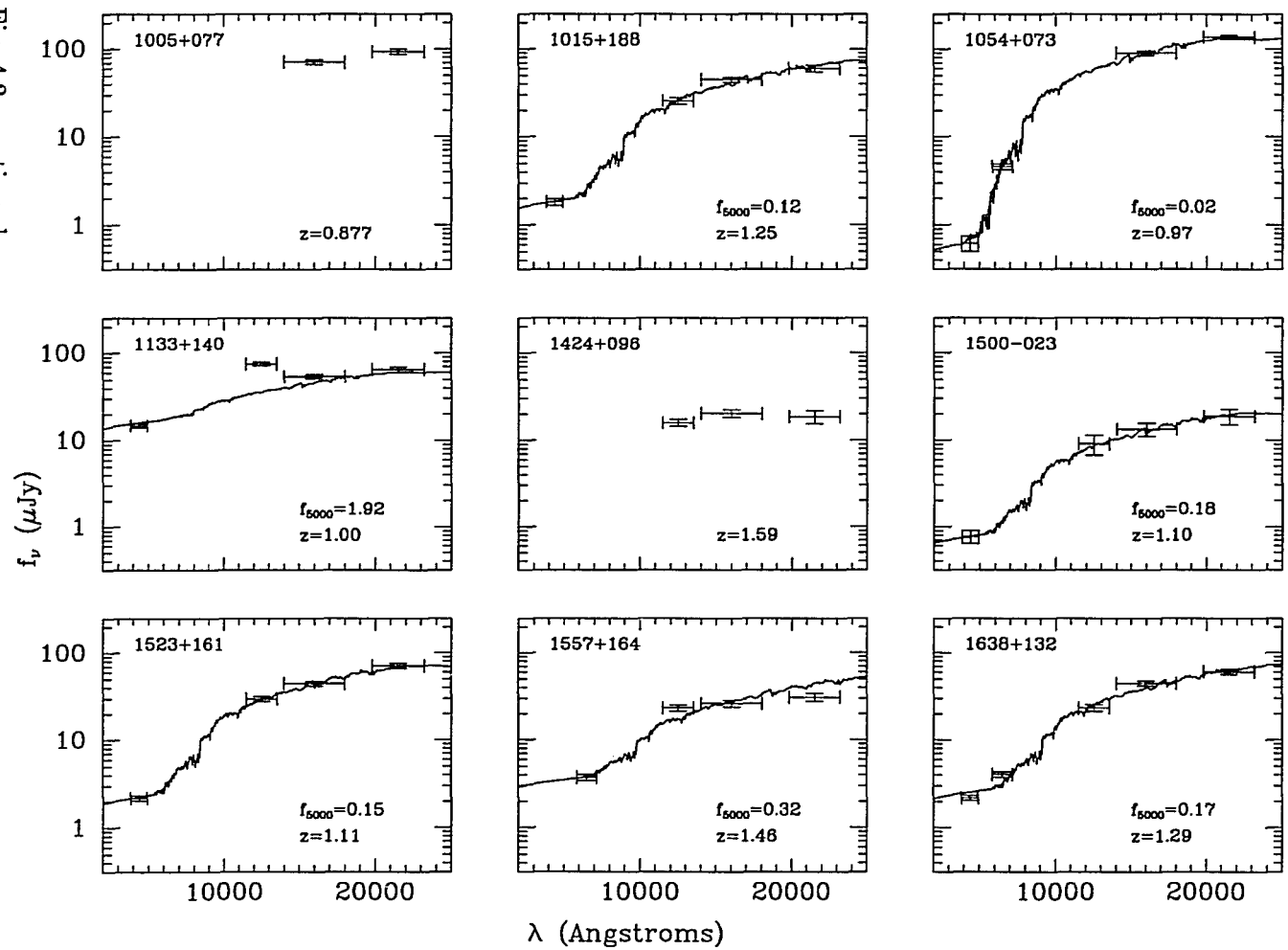

Fig. 4.2- continued.

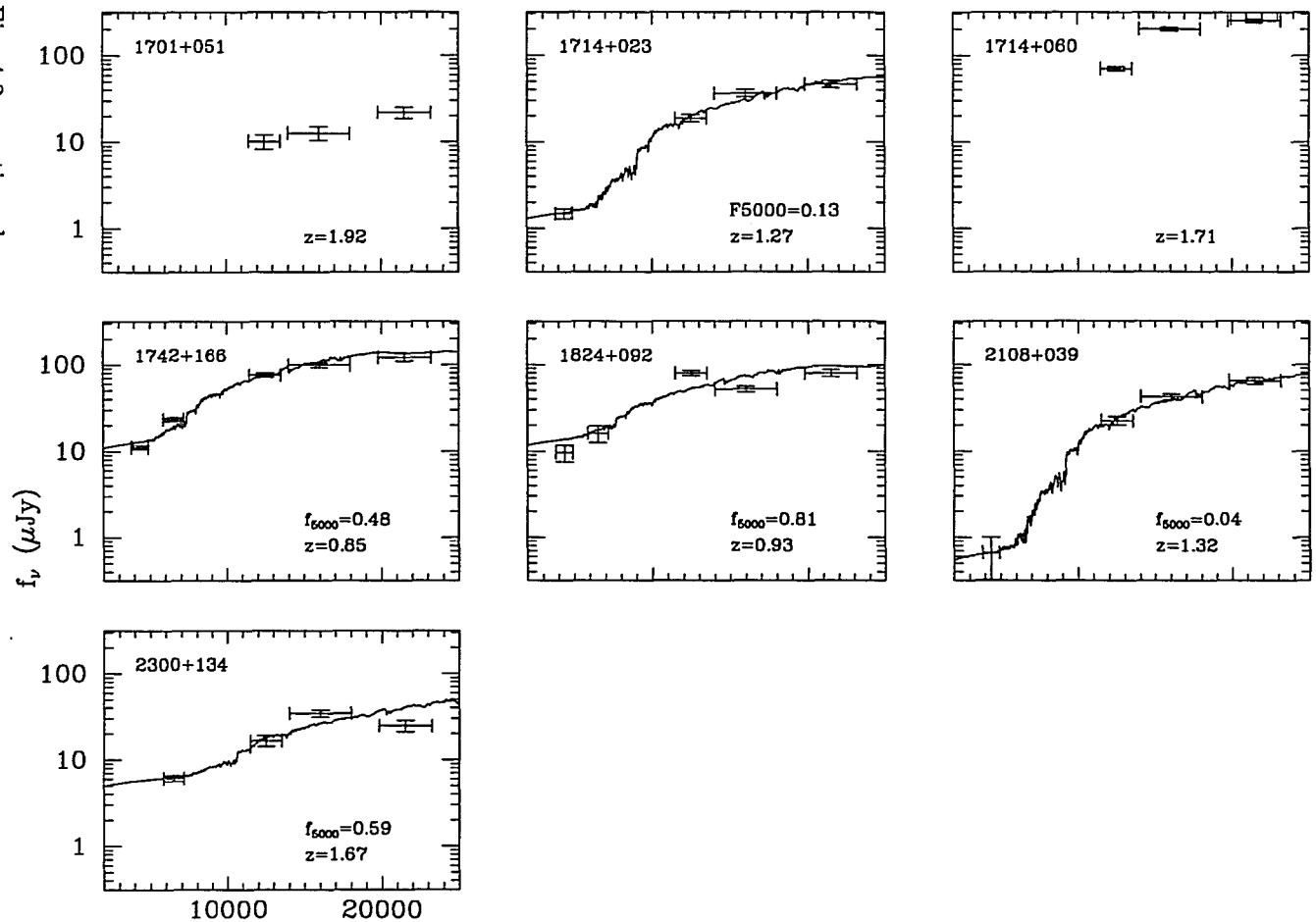

Fig. 4.2– continued.

existence of such a correlation. A study of 3CR galaxies (Lilly 1989) showed no correlation. A recent study of lower radio-luminosity galaxies from the PSR (Dunlop & Peacock 1993) advocates that the PSR galaxies are significantly redder than the 3CR galaxies. For consistency, we have recomputed f_{5000} for the PSR sample using the 2 SED components described above. We derive values of f_{5000} that are 50% higher than those of the original authors. This is caused by the fact that our red SED is redder than theirs. This is not a cause for concern as long as any intercomparisons of f_{5000} are referenced to the same SEDs.

We also recompute f_{5000} for the 3CR comparison sample used by Dunlop & Peacock (1993). Unfortunately this sample consists of only R and K photometry. Ideally we would like to have a 3CR sample with multiple IR bands and CCD bands all measured in the same size aperture. There is currently no such homogeneous sample, so we will make use of the existing more limited data set. As a check, we computed f_{5000} based on only the R and K photometry for the MG sample and found a bias towards larger values of f_{5000} for the restricted set of photometry. It appears that the reasons for this are that 1) the observed IR colors are bluer than the red model SED and 2) the $B-R$ colors are redder than the model. These 2 factors both conspire to produce larger values of f_{5000} when the B, J, and H bands are excluded. To compensate we have multiplied all the 3CR values of f_{5000} by 0.7.

Figure 4.3 shows the derived values of f_{5000} vs. the 2.7 GHz radio power. We see that there are several MG galaxies which are just as blue as their 3CR counter parts. In contrast there are no blue galaxies in the PSR sample. Figure 4.3 seems to show a sharp cutoff at $\log P_{2.7} = 25.8\,\mathrm{W\,Hz^{-1}\,ster^{-1}}$, below which no blue galaxies are produced. If we consider the median value of f_{5000} the values for the 3CR, MG, and PSR samples are 0.27, 0.18, and 0.10 respectively. So the "typical" galaxy gets redder as the radio power is reduced.

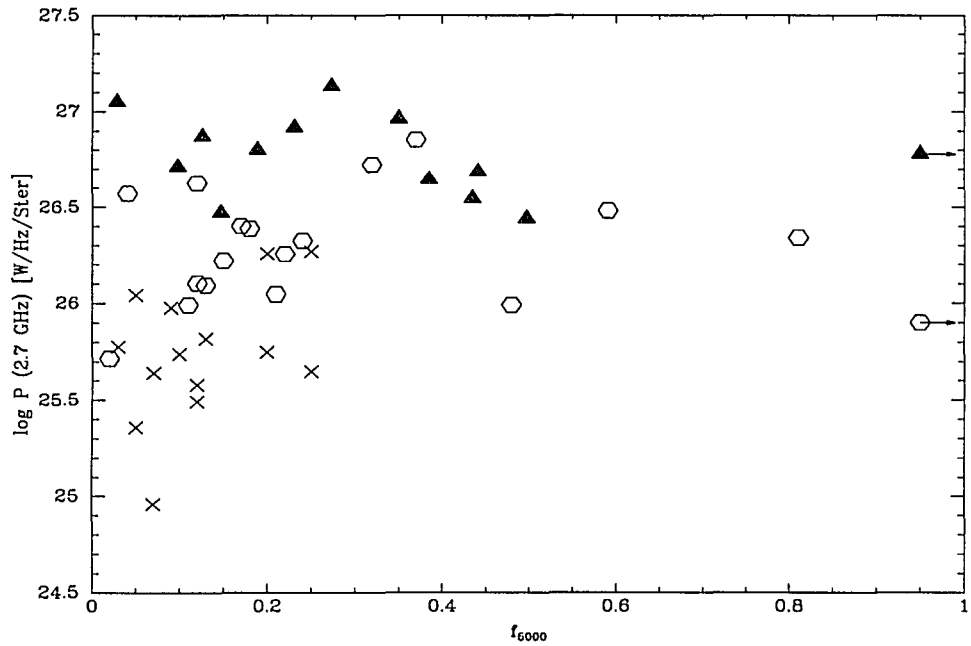

Fig. 4.3.—
Fit values of f_{5000} vs. 2.7 GHz radio luminosity. Triangles are the 3CR sample from Dunlop & Peacock (1993); open symbols are the MG sample; and × represents the PSR sample (Dunlop & Peacock 1993).

We can evaluate the significance of the differences between the distributions using the Kolmogorov-Smirnov (KS) test. The KS statistic is the largest separation between the two normalized cumulative distributions. We ask the question, "What is the probability of having two distributions with a KS statistic at least as large as that observed if they came from the same parent distribution?" A small probability means that it is likely that the two observed distributions came from different parents. The resulting probabilities between pairs of the three distributions are: MG vs. PSR – 0.18, MG vs. 3CR – 0.83, PSR vs. 3CR – 0.04. In other words, we cannot conclude from this test that the MG and 3CR samples are significantly different. Note, however, that the KS test (or any other statistical test) cannot

prove that the two distributions do come from the same parent distribution. So we are left with a tantalizing trend that the median f_{5000} decreases with radio power, but the samples are not quite large enough to make the case unequivocally.

The redshifts for the PSR sample are not spectroscopic and are based on the f_{5000} fits done by Dunlop & Peacock (1993). We now evaluate whether the suggested correlation of P vs. f_{5000} seen in these galaxies is artificially caused by jointly fitting f_{5000} and z. As a test of this, we have arbitrarily added 0.5 to the original estimate of z and rerun the fits. This causes the mean value of f_{5000} in the PSR sample to rise from 0.12 to 0.19. This is still significantly less than the mean of 0.34 seen in the MG sample. Since it is unlikely that the estimated redshifts are that drastically off, and even then such an error would not account for the difference in f_{5000}, we conclude that the difference between the PSR and MG samples is not induced by the lack of spectroscopic redshifts.

4.3.2 Hubble Diagram

We now address the question of whether these galaxies fall on the K-Hubble diagram in the same place as more powerful radio galaxies. Figure 4.4 shows the K magnitudes from this sample (points with error bars) superimposed on 3CR data generously provided by P. McCarthy (private communication). Most of these data appear in his recent review article (McCarthy 1993) and are measured through apertures with diameters ranging from 7″ to 13″. The MG magnitudes are measured through 8″ diameter apertures. No aperture corrections (Sandage 1972) have been applied. Although the brightest MG galaxies are as bright as the brightest 3CR galaxies, the majority of MG galaxies are fainter than 3CR galaxies at the same redshift.

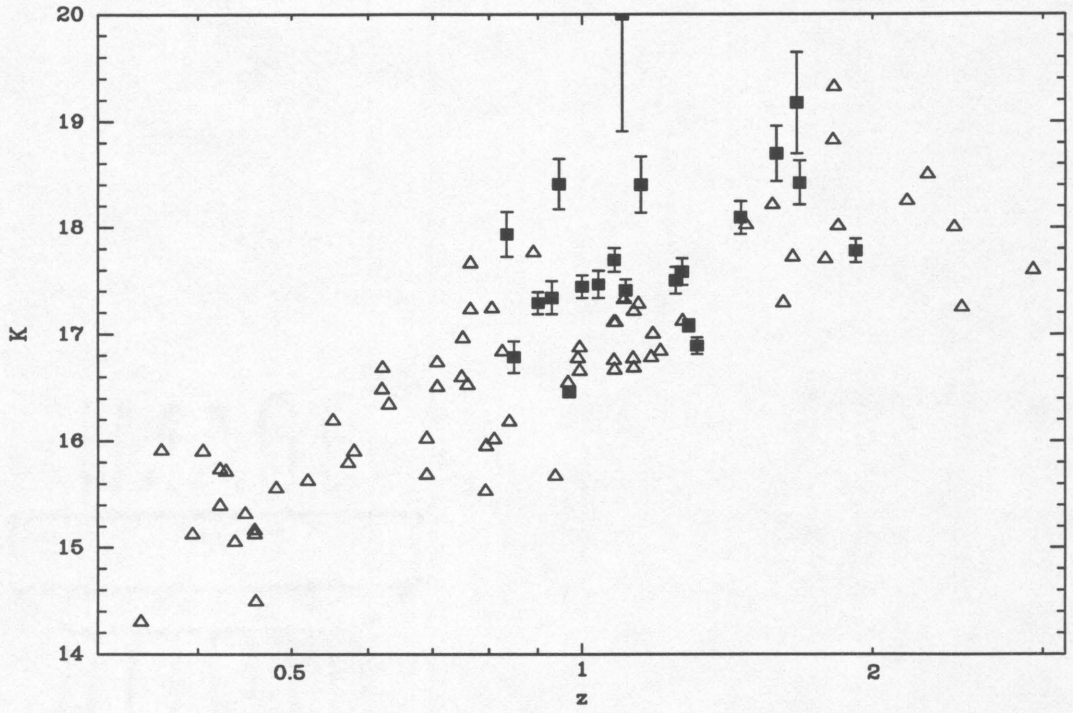

Fig. 4.4.—
K-Hubble diagram. Triangles are 3CR data provided by P. McCarthy. Squares are MG data measured in 8″ apertures.

To address the question of K vs. radio luminosity more quantitatively we now restrict the redshift range to $0.8 < z < 1.3$. We assume $q_0 = 0.5$ and $H_0 = 50\,\mathrm{km\,s^{-1}\,Mpc^{-1}}$ for consistency with other authors – the results are independent of this choice. We have applied a k-correction of -0.67, appropriate for an elliptical galaxy in this redshift range. The SEDs fit in the previous section confirm that this is a reasonable assumption. Furthermore, at K, the k-correction is independent of galaxy type to first order. The 2.7 GHz radio fluxes were obtained from NED[2]. When no 2.7 GHz measurement was listed, the value was interpolated from the 1.4 and 5 GHz measurements, assuming

[2]The NASA Extragalactic Database

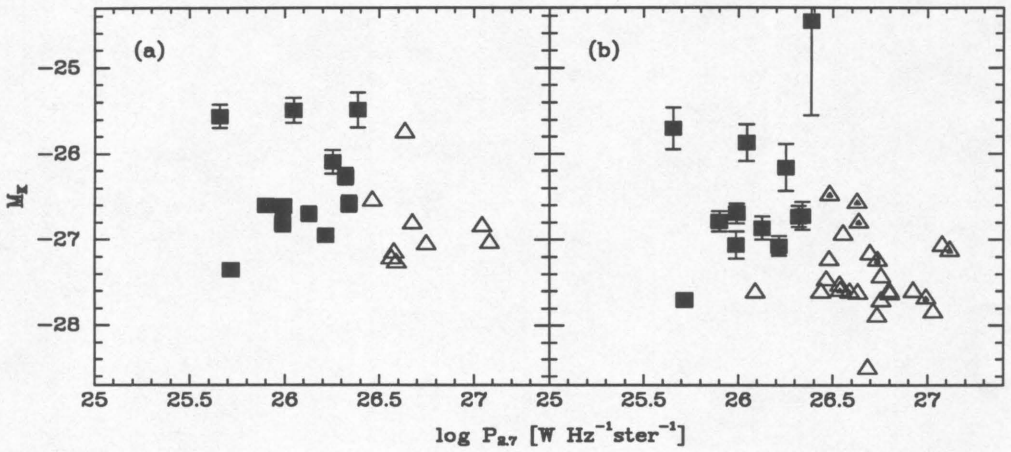

Fig. 4.5.—
Absolute K mag vs. 2.7 GHz radio luminosity. MG data are squares; 3CR data are triangles. (a) K mags are measured in 4″ apertures. The 3CR data come from Rigler et al. (1992). (b) K mags are measured in 8″ apertures. 3CR data come from sources described in text. The galaxies used in panel (a) are marked with dots.

a power-law spectrum. The radio luminosity in W Hz^{-1} ster^{-1} is given by $\log P = D/2.5 + 8.98 + \log S[\mathrm{Jy}] + (\alpha^5_{1.4} - 1)\log(1+z)$, where D is the distance modulus and the last term is the k-correction for a spectrum of the form $S \propto \nu^{-\alpha}$.

Figure 4.5(a) shows the absolute K magnitudes for the MG data and for the 3CR sample of Rigler et al. (1992) measured in 4″ diameter apertures. No correlation of M_K with P is apparent. Panel (b) shows the same quantities for fluxes measured in 8″ apertures. The 3CR photometry here comes from Dunlop & Peacock (1993) (3C 22, 54, 114, 124,173, 208.1, 210, 217, 252, 266, 267, 280, 289, 324, 256, and 368), Lebofsky & Eisenhardt (1986) (3C6.1 and 184), Lilly &

Longair (1984) (3C65, 163.1, and 352), Puschell, Owen, & Laing (1982) (3C265), and this work (3C237 = MG1005+077). Note that 3C 22 is variable (M. Rieke, private communication) and very compact, and so is very quasar-like. Photometry for 3C 226 and 272 comes from the MMT IR photometer (M. Rieke, unpublished). No 8″ aperture photometry was found for the remaining galaxies in this redshift range (3C175.1, 194, 268.1, 300.1, and 305.1). The result here is quite striking:in 8″ apertures the low luminosity radio galaxies have fainter K absolute magnitudes than the high luminosity galaxies.

This can be interpreted in the following way. Within 20 kpc (2″ at $z = 1$) from the centers of the galaxies, the MG and 3CR galaxies have comparable absolute magnitudes. Outside of this region, the 3CR galaxies are more likely to have extended emission or companion galaxies. A cursory comparison of the K images in Figure 4.1 with those of 3CR galaxies (Rigler et al. 1992; Dunlop & Peacock 1993) confirms this.

Statistical tests of the M_K vs. P data show that there is little doubt that there is a correlation in the 8″ data. The KS probability that the absolute K magnitudes of the 3CR and MG data come from the same distribution is 5×10^{-4}. The probability that the 4″ magnitudes are from the same parent distribution is 0.04, implying a weak difference not detected by the eyeball test. We can also evaluate whether the 4″ magnitudes are correlated as strongly as the 8″ magnitudes. As a simple test, we add 0.9, the mean difference between the 3CR and MG 8″ distributions, to the 4″ 3CR magnitudes. If the two distributions are the same, this modified distribution should match the 4″ MG distribution. The KS probability of a match is 0.06. To sum up, the 8″ magnitudes are strongly correlated with radio power. The 4 arsec magnitudes likely have a much weaker correlation, though the small sizes of the samples do not entirely rule out stronger or complete lack of

correlations.

There are two potential explanations for this effect. First, the radio source could somehow be causing the extra emission around the galaxies. It is difficult to explain why the extra emission should be concentrated in the outer parts of the galaxy rather then close to the center. A more natural explanation is that radio sources are generated in galaxies undergoing interactions. An analysis of lower redshift radio galaxies (Heckman et al. 1986) showed that a significant fraction of their sample had disturbed morphologies implying interactions. The radio emission is the result of AGN phenomena fed by gas from the interacting galaxies. Similarly, radio loud quasars are seen to be in denser environments that radio quiet quasars (Ellingson et al. 1991). All these scenarios are consistent with radio phenomena being correlated with the close environments of the host galaxy.

4.4 Summary

We have seen that the SEDs of the MG galaxies are consistent with the IR light being dominated by stars. As a whole, the 3CR, MG, and PSR samples form a progression towards redder galaxies as the radio power decreases. However, there are several MG galaxies that are just as blue as the 3CR galaxies. The three bluest MG galaxies are mostly likely broad-line objects and may have substantial nuclear contamination.

Analysis of the absolute K magnitudes of the MG galaxies at $z = 1$ show that in small apertures (20 kpc radius) they are *not* noticeably fainter than a comparable sample from the 3CR catalog. In contrast, in 40 kpc apertures, the MG galaxies are almost 1 mag fainter. This is consistent with a picture where the environments of the radio galaxies are strongly correlated with the radio power.

Chapter 5

CONCLUDING REMARKS

One of the most important next steps in modeling galaxy distributions will be making use of surface brightness corrected luminosity functions to model the local population of galaxies. The analysis of a LSB population in §3.6.3 is an important first step, but a more accurate treatment should be possible soon (Impey, private communication). I suspect that such a treatment will confirm that surface-brightness selection effects can account for $n(B_J)$ for $B_J < 23$.

At fainter magnitudes, I believe that increasing the number of starbursts will still be necessary. In the present models we considered the extreme situation of a given galaxy having only a single burst in its life. The result showed that with a normal IMF, these bursts leave remnants that should be detected nearby but are not accounted for in the local LF. Using a truncated IMF allows the galaxies to fade sufficiently. However, these model burst populations are all too blue in their $B_J - R_F$ colors implying that the observed galaxies must also have an older red population. Wyse & Silk (1987) have argued that such bimodal star formation may have occurred in the solar neighborhood. Unfortunately, the presence of an

old population exacerbates the lack-of-fading problem. Further analysis will be required to evaluate this scenario.

Closely coupled to the issue of starbursts is that of interactions and merging (Larson & Tinsley 1978; Carlberg & Charlot 1992). Incorporating merging into the modeling problem is complicated because an interaction changes the total number of galaxies, the amount of light (through induced star-formation) and potentially the scale-lengths of the light. Yoshii (1993) has suggested that pre-merger galaxies will not be detected due to surface brightness selection effects. In particular he argues that premergers cannot account for the number of galaxies required to make an $\Omega = 1$ cosmology fit the B_J and K counts as is suggested by Broadhurst et al. (1991).

The starburst treatment that we have introduced is a good starting approximation to increased merging in the past. Our starburst galaxies represent the post-merger galaxies. An useful addition to the modeling program will be to add the number evolution associated with merging to the existing code. This will be especially important in investigating the apparent inconsistencies with the passive evolution model and the colors and redshifts of faint K-selected samples.

Another current deficiency is the state of the $n(m)$ data. Tables 3.1–3.5 are compiled from over two dozen separate sources, each with its own detection criteria, which are often not stated completely. To make matters more complicated, many different filters have been used. With large format CCD mosaics becoming available it is worth considering redoing large parts of the observations in a consistent manner. The ideal survey would image the same areas of the sky in multiple filters, providing color information for a large number of galaxies, and reducing discrepancies introduced by large scale structure. At the same time, the surface

brightness selection criteria could be done in a consistent way, thus eliminating some of the difficulties in analyzing published data sets.

With the radio galaxies there is much yet to be mined from the data set. The morphologies of the galaxies can be analyzed to evaluate the strength of the alignment effect. Simultaneously we can look at the colors of the galaxies as a function of radius. On a larger scale, the environments of the radio galaxies can be studied in some more detail. A comparison of the counts of the surrounding galaxies compared with the data from Chapter 2 will measure the amount of clustering.

Finally, I conclude with some thoughts on what high-resolution imaging will contribute to our understanding of both field and radio galaxies. High-resolution imaging from the ground and space will significantly increase our understanding of the morphologies and close environments of distant galaxies. This will be particularly useful in understanding the role of interactions in both radio and field galaxy phenomena. The best visible wavelength imaging will primarily come from *Hubble Space Telescope*. Ground-based K-band imaging will be able to attain $0\farcs3$ FWHM with simple adaptive optics systems in the short term and $0\farcs1$ in a few years with new large telescopes with full adaptive optics. These tools will be excellent for understanding the near environments and the degree of point source contamination in distant radio galaxies, thus permitting a better analysis of the stellar populations in the galaxies.

REFERENCES

Bahcall, J. N. and Soniera, R. M. 1981, ApJS, 47, 357

Bennet, A. S. 1962, MemRAS, 68, 163

Bennett, C. L., Lawrence, C. R., Burke, B. F., Hewitt, J. N., & Mahoney, J. 1986, ApJS, 61, 1

Bingelli, B., Sandage, A., & Tammann, G. A. 1988, ARA&A, 26, 509

Broadhurst, T. J., Ellis, R. S., & Glazebrook, K. 1992, Nature, 355, 55

Brown, G. S., & Tinsley, B. M. 1974, ApJ, 195, 555

Bruzual A., G., and Charlot S. 1993, ApJ, 405, 538

Burstein, D., & Heiles, C. 1982, ApJ87, 1165

Carlberg, R. G., & Charlot , S. 1992, ApJ, 397, 5

Christian., C. A., Adams, M., Barnes, J. V., Butcher, H., Haynes, D. S., Mould, J. R., & Siegel, M. 1985, PASP, 97, 363

Charlot, S., Ferrari, F., Mathews, G. J., & Silk, J. 1993, ApJ, 419, L57

Ciardullo, R., ApJ, 321, 607

Coleman, G. D., Wu, C.-C., Weedman , D. W. 1980, ApJS, 43, 393

Colless, M., Ellis, R. S., Broadhurst, T. J., Taylor, K., & Peterson, B. A. 1993, MNRAS, 261, 19

Colless, M., Ellis, R. S., Taylor, K., & Hook, R. N. 1990, MNRAS, 244, 408

Colless, M., Schade, D., Broadhurst, T. J., Ellis, R. S. 1994, MNRAS, in press

Cowie, L. L. 1991, in Observational Tests of Inflation, ed. T. Shanks, (Kluwer: Dordrecht), 25

Dalcanton, J. J. 1993, ApJ, 415, L87

Dunlop, J. S., & Peacock, J. A. 1993, MNRAS, 263, 936

Eisenhardt, P., & Chokshi, A. 1990, ApJ, 351, L1

Eisenhardt, P., & Lebofsky, M. J. 1987, ApJ, 316, 70

Elias, J. H., Frogel, J. A., Matthews, K., & Neugebauer. G. 1982, AJ, 87, 1029

Ellingson, E., Yee, H. K. C., & Green, R. F. 1991, ApJ, 371, 49

Elston, R., Rieke, G., and Rieke, M. 1990, in Astrophysics with Infrared Arrays, ed R. Elston (ASP Conf. Ser., 14), 3

Elston, R. 1994, in Infrared Astronomy with Arrays: The Next Generation, ed. I. McLean, (Dordrecht: Kluwer), 33

Fish, R. A. 1964, ApJ, 139, 284

Gardner, J. L., Cowie, L. L. ,& Wainscoat, R. J. 1993, ApJ, 415, L9

Glazebrook, K., Peacock, J. A., Collins, C. A., & Miller, L. 1993 MNRAS, 266, 65

Guhathakurta, P., Tyson, J. A., & Majewski, S. R. 1990 in Evolution of the Universe of Galaxies – The Edwin Hubble Centennial Symposium, ed. R. G. Kron (San Francisco: ASP), 304

Gullixson, C.A., Boeshaar, P. C., Tyson, J. A., Seitzer, P. 1995, ApJS, in press

Gunn, J. E., & Knapp, G. R. 1993, in Sky Surveys: Protostars to Protogalaxies, ed. B. T. Soifer (ASP Conf. Ser., 43), 267

Hall, P., & Mackay, C. D. 1984, MNRAS, 210, 979

Heckman, T. M., Smith, E. P., Baum, S. A., van Breugel, W. J. M., Miley, G. K., Illingworth, G. D., Bothun, G. D., & Balick, B. 1986, ApJ, 311, 526

Heydon-Dumbleton, N. H., Collins, C. A., & MacGillivray, H. T. 1989, MNRAS, 238, 379

Hintzen, P., Romanishin, W., & Valdes, F. 1991, ApJ, 366, 7

Hubble, E. 1936, ApJ, 84, 517

Impey, C. D. 1993, in Sky Surveys: Protostars to Protogalaxies, ed. B. T. Soifer (ASP Conf. Ser., 43), 145

Jarvis, J. F. and Tyson, J. A. 1981, AJ, 86, 476

Johnson, H. L. 1966, ARA&A, 3, 193

Jones, L. R., Fong, R., Shanks, T., Ellis, R. S., Peterson, B. A. 1991, MNRAS, 249, 481

Koo, D. C. 1986, ApJ, 311, 651

Koo, D. C., Gronwall, C., & Bruzual A., G., ApJ, 415, L21

Koo, D. C, and Kron, R. G. 1992, ARA&A, 30, 613

Landolt A. U. 1983, AJ, 88, 439

Landolt A. U. 1992, AJ, 104, 340

Larson, R. B. & Tinsley, B. M. 1978, ApJ, 381, 14

Lebofsky, M. J., & Eisenhardt, P. R. 1986, ApJ, 300, 151

Lilly, S. J., 1989, ApJ, 340, 77

Lilly, S. J 1993, ApJ, 411, 501

Lilly, S. J., Cowie, L. L., & Gardner, J. P., 1991, ApJ, 369, 79

Lilly, S. J. & Longair, M. S. 1984, MNRAS, 211, 833

Loveday, J., Peterson, B. A., Efstathiou, G., & Maddox, S.J. 1992, ApJ, 390, 338

Maddox, S. J., Efstathiou, G., & Sutherland, W. J. 1990, MNRAS, 246, 433

Maddox, S. J., Sutherland, W. J., Efstathiou, G., Loveday, J., Peterson, B. A. 1990, MNRAS, 247, 1P

Majewski, S. R., 1989, in The Epoch of Galaxy Formation , ed. C. S. Frenk, R. S. Ellis, T. Shanks, A. F. Heavens, & J. A. Peacock (Dordrecht: Kluwer), 85

Maoz D. & Rix H.-W. 1993, ApJ, 416, 425

McCarthy, P. J. 1993, ARA&A, 31, 639

McGaugh, S. S. 1992, PhD thesis, University of Michigan

McGaugh, S. S. 1994, Nature, 367, 538

McGaugh, S. S. and Bothun, G. D. 1994, AJ, 107, 530

Metcalfe, N., Fong, R., Shanks, T., & Kilkenny, D. 1989, MNRAS, 236, 207

Metcalfe, N., Shanks, T., Fong, R., & Jones, L. R. 1991, MNRAS, 249, 498

Mobasher, B., Ellis, R. S., & Sharples, R. M. 1986, MNRAS, 223, 11

Montgomery, J. W. and Janes, C. C. 1986, Proc. SPIE 628, 24

Neuschaefer, L. W., Windhorst, R. A., & Dressler, A., 1991, ApJ, 382, 32

Odewahn, S. C., Bryja, C., & Humphreys, R. M. 1992, PASP, 104, 553

Pennington R. L., Humphreys, R. M., Odewahn, S. C., Zumach, W., and Thurmes, P. M. 1993, PASP, 105, 521

Peterson, B. A., Ellis, R. S., Kibblewhite, E. J., Bridgeland, M. T., Hooley, T., & Horne, D. 1979, ApJ, 233, L109

Picard, A. 1991, AJ, 102, 445

Puschell, J. J., Owen, F. N., Laing, R. A. 1982, ApJ, 257, L57

Rigler, M. A., Lilly, S. J., Stockton, A., Hammer, F., & Le Fèvre, O. 1992, ApJ, 385, 61

Salpeter, E. E. 1955, ApJ, 121, 161

Sandage, A. 1961, ApJ, 134, 916

Sandage, A. 1982, ARA&A, 26, 561

Schechter, P., 1976 ApJ, 203, 297

Sebok, W. K. 1986, ApJS, 62, 301

Shanks, T. 1990, in Galactic and Extragalactic Background Radiation, ed. S. Boyer & C. Leinert (Dordrecht: Reidel), 269

Soifer, B. T., et al. 1994, ApJ, 420, L1

Songaila, A., Cowie, L. L., Hu, E. M., & Gardner, J. P. 1994, ApJS, in press

Spinrad H., Dickinson, M., Schlegel, D., & Gonzalez, R. 1993, in Observational Cosmology, ed. G. Chincarini, et al. (ASP Conf. Ser., 51), 585

Stevenson, P. R. F, Shanks, T., & Fong, R. 1986, in Spectral Evolution of Galaxies, ed. C. Chiosi, & A. Renzini (Dordrecht: Reidel), 439

Thuan T. X. & Gunn, J. E. 1976, PASP, 88, 543

Tyson, J. A., 1988, AJ, 96, 1

Valdes, F. 1982, Faint Object Classification and Analysis System (Tucson: NOAO)

van der Kruit, P. C. 1987, A&A, 173, 59

Wainscoat, R. J., Cohen, M., Volk, K., Walker, H. J., and Schwartz, D. E. 1992, ApJS, 83, 111

Wyse, R. F. G., & Silk, J. 1987, ApJ, 313, L11

Yee, H. K. C., Green, R. F., & Stockman, H. S. 1986, ApJS, 62, 681

Yoshii,Y. 1993, ApJ, 403, 552

Yoshii, Y., & Takahara, F. 1988, ApJ, 326, 1

This manuscript was prepared with the AAS LaTeX macros v3.0.